



Net ozone production and its relationship to NO_x and VOCs in the marine boundary layer around the Arabian Peninsula

Ivan Tadic¹, John N. Crowley¹, Dirk Dienhart¹, Philipp Eger¹, Hartwig Harder¹, Bettina Hottmann¹, Monica Martinez¹, Uwe Parchatka¹, Jean-Daniel Paris², Andrea Pozzer^{1,4}, Roland Rohloff¹, Jan Schuladen¹, Justin Shenolikar¹, Sebastian Tauer¹, Jos Lelieveld^{1,3}, and Horst Fischer¹

¹Atmospheric Chemistry Department, Max Planck Institute for Chemistry, Mainz, Germany

²Laboratoire des Sciences du Climat et de l'Environnement, LSCE/IPSL, CEA-CNRS-UVSQ, Université Paris-Saclay, Gif-sur-Yvette, France

³Energy, Environment and Water Research Center, The Cyprus Institute, Nicosia, Cyprus

⁴International Centre for Theoretical Physics, Trieste, Italy

Correspondence to: Ivan Tadic (i.tadic@mpic.de)

Abstract. Strongly enhanced tropospheric ozone mixing ratios have been reported in the Arabian Basin, a region with intense solar radiation and high concentrations of ozone precursors such as nitrogen oxides and volatile organic compounds. To analyze photochemical ozone production in the marine boundary layer (MBL) around the Arabian Peninsula, we use ship-borne observations of NO , NO_2 , O_3 , OH , HO_2 , HCHO , actinic flux, water vapor, pressure and temperature obtained during the summer 2017 Air Quality and Climate in the Arabian Basin (AQABA) campaign, compare them to simulation results of the ECHAM-MESSy atmospheric chemistry (EMAC) general circulation model. Net ozone production rates (NOPR) were greatest over the Gulf of Oman, the Northern Red Sea and the Arabian Gulf with median values of $14 \text{ ppb}_v \text{ day}^{-1}$, $16 \text{ ppb}_v \text{ day}^{-1}$ and $28 \text{ ppb}_v \text{ day}^{-1}$, respectively. NOPR over the Mediterranean, the Southern Red Sea and the Arabian Sea did not significantly deviate from zero; however, results for the Arabian Sea indicate weak net ozone production of $5 \text{ ppb}_v \text{ day}^{-1}$, and net ozone destruction over the Mediterranean and the Southern Red Sea with $-2 \text{ ppb}_v \text{ day}^{-1}$ and $-4 \text{ ppb}_v \text{ day}^{-1}$, respectively. Constrained by measured HCHO/NO_2 -ratios, our photochemistry calculations show that net ozone production in the MBL around the Arabian Peninsula occurs mostly in a transition regime between NO_x - and VOC-limitation with a tendency towards NO_x -limitation except over the Northern Red Sea and the Oman Gulf.



1 Introduction

Revenues from exploitation of the great oil reserves in the states of and around the Arabian Peninsula have propelled remarkable economic development associated with industrialization and urbanization. Strong population growth and anthropogenic emissions of gases and particulates in the last few decades have resulted in the Middle East becoming a hotspot for air pollution and associated health effects, while it is also one of the regions worldwide where climate change is particularly rapid (Lelieveld et al., 2016a). Unique meteorological conditions such as intense solar radiation, high temperatures and aridity, as well as strong anthropogenic emissions of volatile organic compounds (VOCs) and NO_x ($= \text{NO} + \text{NO}_2$) by on- and off-shore petrochemical industries, dense ship traffic, fossil energy production for air conditioning and desalination, and urban development are expected to further intensify in the future and contribute to photochemical ozone production (Lelieveld et al., 2009; Krotkov et al., 2016; Pfannerstill et al., 2019). Understanding the sources and sinks of NO_x and other ozone precursors on and around the Arabian Peninsula is therefore of major importance for atmospheric chemistry studies, including the investigation of net ozone production rates (NOPR) (Monks et al., 2015; Reed et al., 2016; Bozem et al., 2017).

NO_x plays a central role in atmospheric photochemistry (Nakamura et al., 2003; Tuzson et al., 2013; Reed et al., 2016). It is the primary precursor for tropospheric ozone (O_3), secondary organic aerosols and photochemical smog in urban areas (Hollaway et al., 2012; Javed et al., 2019). Main ground-based sources of NO and NO_2 are fossil fuel combustion and to a lesser extent bacterial processes in soils, and both lightning and aircraft emissions in the upper troposphere (Nakamura et al., 2003; Miyazaki et al., 2017; Javed et al., 2019). Transport of NO_x in the atmosphere is relatively limited due to its short lifetime of a few hours (Reed et al., 2016). It is removed from the troposphere mainly by conversion to HNO_3 (via reaction with OH) during the day, or the formation of N_2O_5 (in the reaction of NO_2 with NO_3 at night-time), which also leads to formation of nitric acid by heterogeneous hydrolysis on aerosol surfaces (Crutzen, 1973; Liu et al., 2016; Reed et al., 2016). Ultimately, the deposition of HNO_3 constitutes the major loss process of NO_x from the atmosphere. Ozone is a secondary pollutant that is photochemically formed in the troposphere from its precursors NO_x and VOCs (Bozem et al., 2017; Jaffe et al., 2018). It is an important greenhouse gas, an atmospheric oxidant and the most important primary precursor for OH (Lelieveld et al., 2004; Monks et al., 2015; Bozem et al., 2017). O_3 in the planetary boundary layer causes health damage, notably respiratory diseases, and reduces crop yields (Monks et al., 2015; Jaffe et al., 2018).

NO_x and O_3 mixing ratios in the troposphere vary from less than 20 ppt_v and 10 ppb_v, respectively, for pristine conditions such as the remote marine boundary layer (MBL) up to mixing ratios of several hundreds of ppb_v in regions with heavy automobile traffic and in international shipping lanes (for NO_x) and downwind of urbanized areas (for O_3) (Reed et al., 2016; Jaffe et al., 2018). Low NO_x environments such as the clean MBL and the lower free troposphere are considered net ozone destruction regimes whereas the upper troposphere and areas with anthropogenic emissions of ozone precursors are regions



of net ozone production (Klonecki and Levy, 1997; Bozem et al., 2017). Measurements performed in the Houston Ship Channel revealed that NOPR can be of the order of several tens of ppb h⁻¹ even in marine environments (Zhou et al., 2014).

60 In the last decade much effort has been successfully devoted to the mitigation of NO_x emissions over Europe and America, and levels of reactive nitrogen trace gases have decreased (Miyazaki et al., 2017). But in Asia, India and the Middle East, NO_x emissions have substantially increased during the last decade so that the global NO_x burden has essentially remained constant (Miyazaki et al., 2017). NO_x emissions by ocean-going vessels have attracted considerable attention as they are reported to account for 15 % of the global NO_x emission burden (Celik et al., 2019). Model calculations suggest that the
65 Arabian Gulf, with an estimated annual NO_x emission density of about one ton km⁻² from ship traffic, is among the regions with highest NO_x emission densities worldwide (Johansson et al., 2017). Although NO_x emissions in the Red Sea and Arabian Sea areas were reported to be three and five times smaller than for the Arabian Gulf, respectively, these values are still 50-100 times larger than the emission density reported for the South Pacific Ocean, for example (Johansson et al., 2017).

In the present study, we characterize photochemical NOPR in the MBL around the Arabian Peninsula. In Sect. 2, the
70 campaign, instrument description, data processing and a description of the methods used in this study is presented. In Sect. 3, mixing ratios of nitrogen oxides and ozone around the Arabian Peninsula are reported. Based on concurrent measurements of HO_x, actinic flux, temperature and pressure, noontime RO₂ mixing ratios are estimated and used to calculate NOPR in the different regions around the Arabian Peninsula. Observation-based analysis of HCHO/NO₂-ratios will be used to distinguish between NO_x- or VOC-limited chemistry in the particular regions. A comparison of the results with data retrieved from the
75 3D global circulation model EMAC is also included.

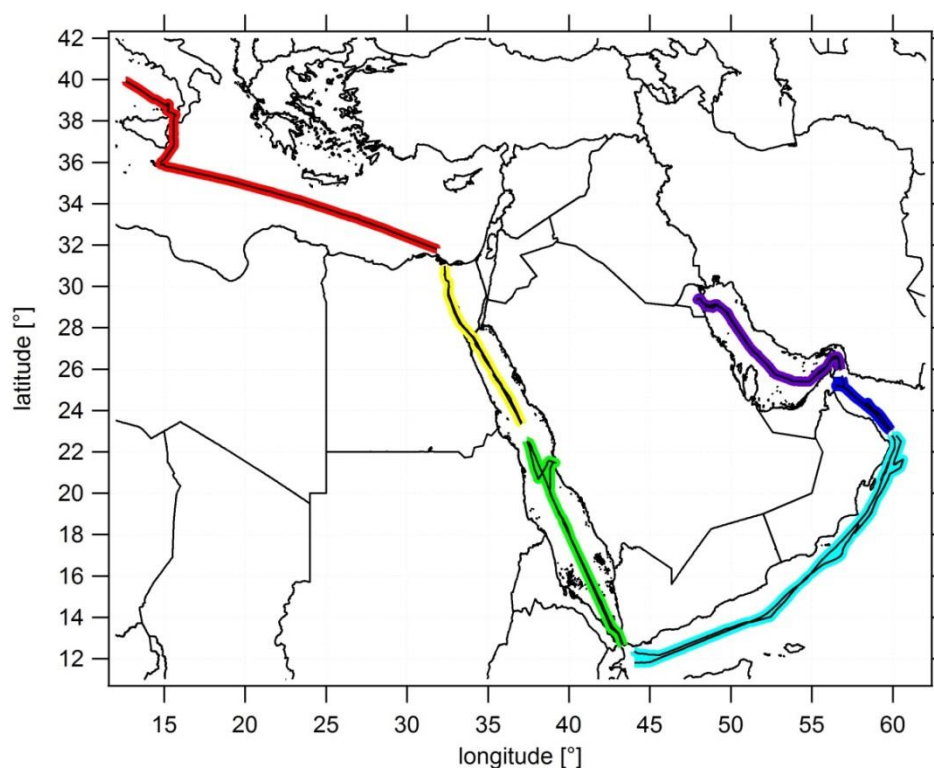
2 Experimental

2.1 AQABA campaign

The AQABA ship campaign (Air Quality and Climate in the Arabian Basin) investigated the chemical composition of the MBL around the Arabian Peninsula. From late June to early September 2017, the *Kommandor Iona* Research and Survey
80 Vessel sailed from Toulon (France) to Kuwait and back in order to perform gas-phase and particle measurements in the region. The gas-phase and aerosol measurement instrumentation was housed in five laboratory containers on the front deck. Trace gases were sampled via a 6 m high, 20 cm diameter cylindrical stainless steel inlet (total mass flow of 10,000 SLM) installed on the front deck of the vessel. Air was drawn at a flow rate of 28.5 SLM into the laboratory container containing the HCHO and NO_x measurements via a ½" PFA tubing (residence times of ~ 4 s). For the other trace gas measurements
85 (excluding H₂O vapor which was measured on the top of the ship mast in the front) sampling was achieved through bypass systems. The OH and HO₂ detection units were placed on the prow to allow for inlets with residence times less than 10 ms.



The *Kommandor Iona* left Malta in late June 2017 traversing the Mediterranean Basin, the Suez Canal and the Northern Red Sea. A 3 day stop-over at KAUST University (Saudi Arabia) was made from July 11th to July 13th before passing the Southern Red Sea area. On July 17th, we briefly stopped at Djibouti port before passing the Gulf of Aden, the Arabian Sea and the Gulf of Oman. Kuwait at the northern end of the Arabian Gulf marked the turning point of the ship cruise where, during a second 3-day stop-over, scientific staff was exchanged. The *Kommandor Iona* started the second leg on August 03rd 2017 arriving in Toulon (France) in early September 2017 without any further stops. Figure 1 shows the ship's route subdivided into six different regimes.



95 **Figure 1: Ship cruises during both legs and color-coded subdivision into six different regimes. The following abbreviations will be used: AG for Arabian Gulf (purple), OG for Oman Gulf (dark blue), AS for Arabian Sea (blue), SRS for Southern Red Sea (green), NRS for Northern Red Sea (yellow), M for Mediterranean (red).**

To enhance the statistical significance of our results and due to comparable signatures of the NO_x and O_3 measurements in the northern part of the Red Sea, the Suez Gulf and the Suez Canal, we have combined these regions which are represented by the ‘Northern Red Sea’ (NRS). For the same reasons we have merged the Gulf of Aden with the Arabian Sea (AS). Table 1 shows the range of latitudinal and longitudinal coordinates of the different regions. See supplementary table ST1 for a detailed day to day description of the route.



105 **Table 1: Range of latitudinal and longitudinal coordinates and dates during both legs of the different regions.**

region (abbreviation)	latitudinal range	longitudinal range	Date (1 st leg)	Date (2 nd leg)
Mediterranean (M)	31.810° N- 39.923° N	12.620° E- 31.850° E	---	25.08.2017 – 31.08.2017
Northern Red Sea (NRS)	23.343° N- 30.986° N	32.305° E- 37.085° E	03.07.2017 – 08.07.2017	21.08.2017 – 24.08.2017
Southern Red Sea (SRS)	12.672° N- 22.494° N	37.411° E- 43.327° E	09.07.2017 – 16.07.2017	17.08.2017 – 20.08.2017
Arabian Sea (AS)	11.797° N- 22.782° N	44.035° E- 60.636° E	18.07.2017 – 24.07.2017	07.08.2017 – 16.08.2017
Oman Gulf (OG)	23.050° N- 25.622° N	56.492° E- 59.913° E	24.07.2017 – 27.07.2017	05.08.2017 – 07.08.2017
Arabian Gulf (AG)	25.396° N- 29.425° N	47.920° E- 56.772° E	27.07.2017 – 31.07.2017	03.08.2017 – 05.08.2017

2.2 Measurements of nitrogen oxides during AQABA

Chemiluminescent detection of NO and NO₂ is a widely applied method to quantify mixing ratios from the ppm_v down to the low ppt_v range (Nakamura et al., 2003; Pollack et al., 2011; Hosaynali Beygi et al., 2011; Reed et al., 2016). During AQABA we deployed a compact, robust and commercially available two-channel chemiluminescence instrument CLD 790 SR (ECO Physics AG, Dürnten, Switzerland) that has been optimized for in situ field measurements during the last decade (Hosaynali Beygi et al., 2011). The measurement principle of the CLD is based on the addition of O₃ to NO to produce stoichiometric quantities of excited state NO₂^{*} that will emit an infrared photon ($\lambda > 600$ nm) forming the chemiluminescent detection principle for NO (Drummond et al., 1985; Reed et al., 2016). Both channels feature an identical layout and were operated at a mass flow of 1.5 SLM during AQABA. One channel of the CLD (NO_c-channel) has additionally been equipped with a LED solid state photolytic converter (Droplet Measurement Techniques, Boulder, Colorado) installed upstream of the O₃ addition to selectively photolyze NO₂ to NO, which is subsequently measured. In this section, we will concentrate on modifications made prior to the campaign and especially on operational conditions of the photolytic converter during the campaign. Further details on the measurement principle are described elsewhere (Pollack et al., 2011; Hosaynali Beygi et al., 2011; Reed et al., 2016).

During AQABA, the cylindrical photolytic converter (length 14 cm, volume 0.079 l) was operated at a constant pressure of 95 hPa yielding a residence time of ~ 0.3 s. The photolytic NO₂ converter features a set of 50 UV LED units attached to each end of the converter. The emission profile of the UV LED units was characterized in laboratory measurements to peak at 398



nm with a Full Width at Half Maximum (FWHM) of 16 nm. UV-induced positive bias in the NO₂ measurements due to
 125 photolysis of HONO, BrONO₂, NO₃ and ClNO₂ to produce NO was characterized ahead of the campaign to be 7.7 %, 7.2 %, 5.6 % and 1.5 % of the respective ambient concentration of HONO, BrONO₂, NO₃ and ClNO₂ respectively, and was neglected for the observations in this study due to small daytime concentrations of these molecules in the MBL. To calculate the UV-induced positive bias we used absorption cross sections from the MPI-Mainz UV/VIS Spectral Atlas of Gaseous Molecules (Keller-Rudek et al., 2013). To limit wall loss of NO₂, the inner cavity surface is made of PTFE
 130 (polytetrafluoroethylene), which may potentially provide a reservoir (via surface adsorption) for NO_y that can thermally dissociate to increase the background signal of the NO₂ measurement (Reed et al., 2016). The conversion efficiency K_e of the photolytic NO₂ conversion was estimated by gas phase titration (SYCOS K-GPT-DLR, ansyco, Karlsruhe, Germany) several times before, during and after the campaign at $(29.4 \pm 0.9) \%$ allowing the calculation of NO₂ concentrations by $[NO_2] = \frac{[NO_c] - [NO]}{K_e}$. To avoid chemical interferences due to adding ozone in excess during a gas phase titration, a small but
 135 not vanishing amount of NO has always been left unoxidized during gas phase titrations.

During AQABA, regular dry zero-air measurements as well as NO and NO₂ calibrations were performed autonomously over a 10 minute period every 6 hours to accurately quantify the instrumental background and to correct for sensitivity drifts. An autonomous cycle of ‘2 min zero air measurements – 2 min NO calibration – 2 min zero air measurement – 2 min NO₂ calibration – 2 min zero air measurement’ was implemented. Continuous flows NO and NO₂ calibration gases were added to
 140 the synthetic airflow or directed to a pump by switching solenoid valves. The NO calibration standard (1.954 ± 0.039 ppm_v NO in N₂, Air Liquide, Germany) used during the campaign was compared to a primary standard (5.004 ± 0.025) ppm_v (NPL, Teddington, UK) after the campaign yielding an effective NO mixing ratio of (2.060 ± 0.057) ppm_v in the NO calibration gas. Both zero air measurements and NO calibrations were performed with a total flow of 3.44 SLM achieving an overflow of 0.44 SLM to guarantee ambient air free standard measurements by adding the calibration gas to the zero air
 145 flow. During AQABA, NO calibrations at 2.5 ppb_v were achieved. During the first leg of the campaign, zero air was sampled from a bottle (Westfalen AG, Germany), whereas during the second leg zero air was generated from a zero air generator (Air Purifier CAP 180, acuraLine). Zero air measurements generated with the zero air generator were statistically not significantly different from those achieved by a bottle. To correctly account for the photomultiplier background and chemical interferences due to reactions of ozone with ambient alkenes additional pre-chamber measurements were
 150 performed every 5 minutes as well as at the beginning of zero air measurements and calibrations for 25 s each. This correction is removing a large fraction of the interference signal from alkenes. However, in regions where alkene concentrations are notably high, the CLD is prone to enhanced backgrounds. A schematic setup of the two-channel CLD instrument is given in Figure 2.

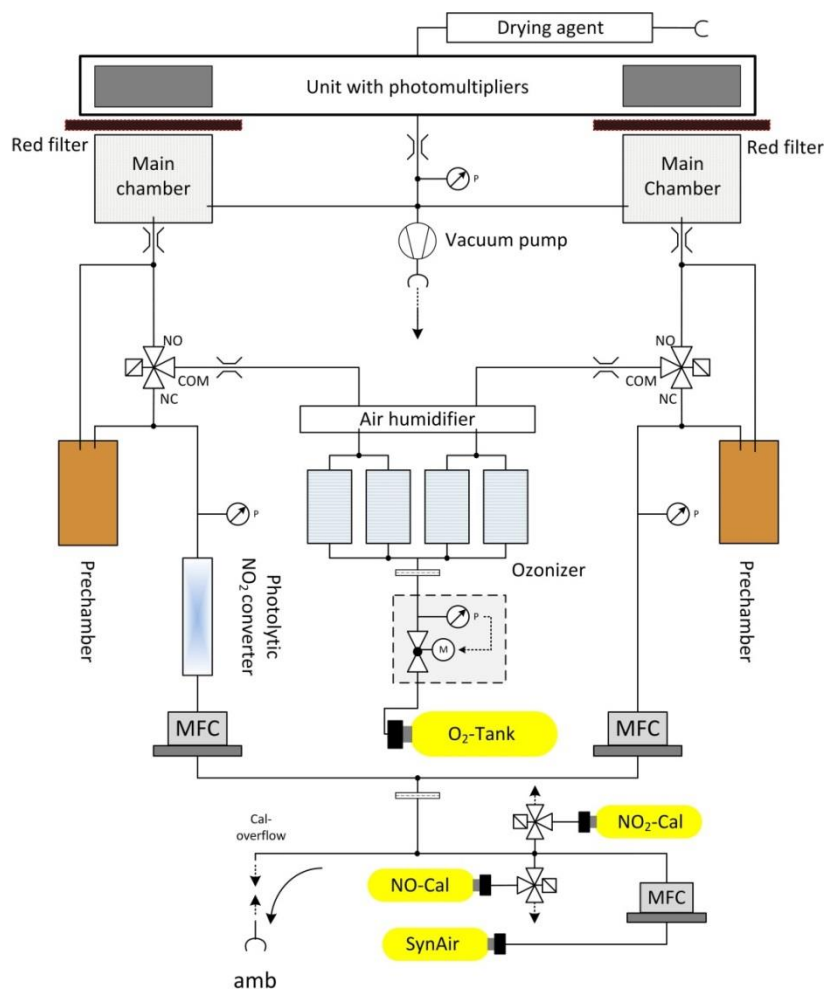


Figure 2: Schematic setup of the two channel CLD instrument in the configuration used during AQABA. NO and NO₂ calibration gases were running continuously and were added to the zero airflow by switching the respective solenoid valves.

The total measurement uncertainty (TMU) in the NO data is 5.5 % at a 5 min integration time and a confidence level of 1σ . The limit of detection in the NO channel was estimated as the full width at half maximum of the frequency distribution of all zero air measurements obtained during the campaign to be 9 ppt_v at a 5 min integration time and a confidence level of 1σ . The TMU in the NO₂ data is $7\% \pm 112$ ppt_v at a confidence level of 1σ and an integration time of 5 min. As the zero air measurements in the NO₂ channel produced an increased background affected by memory effects after exposure to high NO_x levels e.g. during measurements of stack emissions, the NO₂ raw data were initially processed without converter background subtraction. As we therefore expect the CLD NO₂ data to be offset due to not being initially background corrected, the converter background was estimated at 112 ppt_v from the centre of a Gaussian fit representing the difference of 1-minute averaged CLD NO₂ and concurrent cavity ring-down spectroscopy (CRDS) NO₂ measurements for data points below 10 ppb_v as we expect the NO₂ CLD to be offset due to not being background corrected. Setting the threshold for calculating the



difference of the two concurrent data sets to 10 ppb_v is somewhat arbitrary, however, changing this limit to 5 ppb_v or 20 ppb_v does not significantly vary the estimated offset of the CLD NO₂ data. The offset correction of 112 ppt_v was taken as the ultimate absolute measurement uncertainty of the CLD NO₂ measurement. Further corrections of to the final CLD data include residence time corrections as well as corrections for NO and O₃ losses and the subsequent formation of NO₂ in the sampling line (Ryerson et al., 2000). Both NO and NO₂ CLD data have also been corrected for nonlinearities for concentrations higher than 55 ppb_v, as experienced during probing of stack emissions.

2.3 Further measurements used in this study

An extensive set of concurrent measurements providing mixing ratios of O₃, NO₂, HCHO, OH, HO₂, absolute humidity and actinic flux, temperature and pressure data obtained during AQABA was used in this study. Ozone was measured with an absorption photometer (Model 202 Ozone Monitor, 2B Technologies, Boulder, Colorado) based on the well-established absorption of the mercury line in the Hartley band at 254 nm (Viallon et al., 2015). Eliminating water and particle interferences during sampling was achieved via sampling through a nafion tube and a Teflon filter. The ozone monitor was zeroed ten times during the campaign. NO₂ was further measured by cavity ring-down spectroscopy (Sobanski et al., 2016) and used for correcting the instrumental background of the CLD NO₂ data, as described above (the correction was taken as the ultimate absolute measurement uncertainty in the CLD NO₂ data). Note that in this study we will use the NO₂ CLD data rather than the NO₂ CRDS data as the temporal coverage of the CLD NO₂ data over the course of the campaign is about 60 % compared to about 35 % for the cavity ring-down measurement. Formaldehyde (HCHO) was measured with an Aerolaser 4021 (AERO-LASER GmbH, Garmisch-Partenkirchen, Germany), which is a fully automatized monitor based on the Hantzsch technique (Kormann et al., 2003). H₂O measurements were obtained using a cavity ring-down spectroscopy monitor (PICARRO G2401, Santa Clara, California) supervised by Laboratoire des Sciences du Climat et de l'Environnement (LSCE) (Kwok et al., 2015). Measurements of OH and HO₂ were performed with the custom-built **HydrOxyl Radical measurement Unit** based on fluorescence **Spectroscopy** (HORUS) instrument based on laser-induced fluorescence (LIF) spectroscopy of the OH molecule and NO titration of HO₂ to OH followed by LIF spectroscopy detection of the OH molecule (Martinez et al., 2010; Regelin et al., 2013). HO₂ data used in this study is still preliminary due to not yet quantified interference of organic peroxy radicals RO₂. This correction is expected to reduce the final HO₂ concentrations by less than 20 % around noontime, which will not significantly change the results presented here. Wavelength resolved down-welling actinic flux was measured with a spectral radiometer (model CCD Spectroradiometer 85237). The *j*-values for NO₂ and O₃ were not corrected for upwelling UV radiation and were estimated to have a ~ 10 % measurement uncertainty (Meusel et al., 2016). The radiometer was installed 10 m above sea level, respectively 5 m above the front deck surface. Decreases in sensitivity due to sensor contamination with e.g. sea-spray were corrected with a linear interpolation between two (daily) cleaning events. Temperature and pressure measurements were performed with the Shipborne **European Common Automatic Weather Station** (EUCAWS), a weather station specifically designed for ships. The weather station incorporates sensors, processing units, satellite positioning and communication systems in one device and is implemented



and coordinated by the European National Meteorological Service EUMETNET. Table 2 lists the measurement methods and the TMU for each observation.

Table 2: List of observations and gas phase measurements during AQABA. The TMU at a confidence level of 1σ and at the particular temporal resolution as well as a reference of the measurement operability are given.

Molecule	Method	TMU	References
NO	chemiluminescence	6 %	Hosaynali Beygi et al., 2011
NO ₂	photolysis-chemiluminescence	7 %	Hosaynali Beygi et al., 2011
NO ₂	cavity ring-down spectroscopy	7 %	Sobanski et al., 2016
O ₃	UV absorbance	2 %	Viallon et al., 2015
OH	LIF	20 %	Martinez et al., 2010
HO ₂	NO titration / LIF	20 %	Martinez et al., 2010
HCHO	Hantzsch technique	13 %	Kormann et al., 2003
H ₂ O	cavity ring-down spectroscopy	5 %	Kwok et al., 2015
actinic flux	spectral radiometer	10 %	Meusel et al., 2016

The *Kommandor Iona* Research and Survey Vessel sailed whenever possible with the wind coming from the bow to avoid contamination by stack emissions. However, based on the relative wind direction, the variability in NO as well as the temporal evolution of NO_x, SO₂, and O₃ sections of data in which the air mass was contaminated by the ship's stack were identified. All data used here to calculate RO₂ and NOPR have been filtered to remove contaminated air masses. Altogether, 21 % of the sampling time was potentially contaminated by the ship exhaust of the KI of which 87 % occurred on the first leg. During the second leg the ship sailed against the wind and most of the data was free of stack contamination. Our analysis is based on a 5-minute running mean for each data set, whereby only averages that have been calculated at a temporal coverage greater than 30 % have been used. A time series of the NO, NO₂ (both CLD), O₃ and $j(\text{NO}_2)$ measurements is given in the supplements Figures S2 and S3.

NO and NO₂ were measured from July 03rd to August 31st, O₃ was measured from June 22nd to September 01st, HCHO from July 01st to August 31st and OH and HO₂ from July 18th to August 31st. For the analysis of peroxy radicals RO₂ and NOPR around the Arabian Peninsula we have removed data measured during the stop-overs in Jeddah (July 11th to July 13th), Kuwait (July 31st to August 03rd) and during bunkering at Fujairah City (August 06th, 07:00 – 15:00 UTC). Due to HO_x data being available from July 18th onward, we have limited the net ozone production analysis to the period after this date.



2.4 Methods

The so-called $\text{NO}_x\text{-O}_3$ -null cycle represents a rapid daytime cycling between NO, NO_2 and O_3 . Solar UV radiation photolyzes NO_2 to NO and $\text{O}(^3\text{P})$ (R1) which will reform O_3 in the subsequent reaction with molecular oxygen O_2 (R2) (Leighton, 1961). NO and O_3 react to form NO_2 and O_2 (R3). R1, R2 and R3 constitute a so called null cycle which establishes photostationary steady state (PSS) for both NO_x and O_3 in mid latitudes during noon time on a time scale of ~ 100 s (Thornton et al., 2002; Mannschreck et al., 2004).



Under the assumption of PSS, the Leighton Ratio φ is unity (Leighton, 1961)

$$\varphi = \frac{j(\text{NO}_2) \cdot [\text{NO}_2]}{k_{\text{NO}+\text{O}_3} \cdot [\text{NO}][\text{O}_3]} = 1 \quad (1)$$

with $j(\text{NO}_2)$ being the NO_2 photolysis rate [s^{-1}]. In low NO_x environments ($< 100 \text{ ppt}_v$) previous studies have indicated that further NO oxidizing trace gases such as peroxy radicals (HO_2 , RO_2) and halogen monoxides (XO) may result in a deviation from unity (Nakamura et al., 2003; Hosaynali Beygi et al., 2011; Reed et al., 2016).



In the present study we include HO_2 and R_iO_2 into the production term for NO_2 .

$$j(\text{NO}_2) \cdot [\text{NO}_2] = k_{\text{NO}+\text{O}_3} \cdot [\text{NO}][\text{O}_3] + k_{\text{NO}+\text{HO}_2} \cdot [\text{NO}][\text{HO}_2] + [\text{NO}] \cdot \sum_i k_{\text{NO}+\text{R}_i\text{O}_2} \cdot [\text{R}_i\text{O}_2] \quad (2)$$

Assuming that the temperature-dependent rate coefficient for the reaction of each particular peroxy radical R_iO_2 with NO equals the rate $k_{\text{NO}+\text{HO}_2}$ for Reaction R4 (Hauglustaine et al., 1996; Cantrell et al., 1997; Thornton et al., 2002), we can combine HO_2 and the sum of all organic peroxy radicals R_iO_2 to the entity RO_2 that can be estimated using the steady state equation

$$[\text{RO}_2] = \frac{j(\text{NO}_2) \cdot [\text{NO}_2] - k_{\text{NO}+\text{O}_3} \cdot [\text{NO}][\text{O}_3]}{k_{\text{NO}+\text{HO}_2} \cdot [\text{NO}]} \quad (3)$$



However, the steady state assumption is not valid if the sampled air parcel is affected by fresh emissions or fast changes in the actinic flux (Thornton et al., 2002). After sampling a fresh emission e.g. a ship plume, for which NO_x went up typically to values of several tens of ppb_v with simultaneous titration in O_3 , we assume that PSS is re-established on a time scale of 2 minutes (Thornton et al., 2002; Mannschreck et al., 2004). To best approximate PSS in our analysis we have restricted the estimation of RO_2 on time frames ± 2 h around noontime for which we expect the smallest relative changes in the actinic flux. Noontime for each day was determined as the centre of a Gaussian fit that was applied to the actinic flux data. We applied a Gaussian Fit to the actinic flux data as this fitting method is sufficient to estimate the centre of the diurnal actinic flux. To further limit the effect of periods for which PSS is not fulfilled, we use the median instead of the average that is often disproportionately biased by strong NO_x sources nearby. See supplements Tables ST2, ST4 and ST6 for detailed statistics and a further motivation on regional averages and median values. See supplements Figure S1 for a detailed illustration of the calculation of the fraction of the noontime integral.

A further part of the analysis will be the investigation of NOPR. Ozone production is initiated by reactions that produce HO_x , for which primary production is from the photolysis of ozone, formaldehyde, nitrous acid (HONO) and hydrogen peroxide (H_2O_2) (Thornton et al., 2002; Hens et al., 2014; Lu et al., 2016; Mallik et al., 2018). The production of ozone can be approximated by the rate of oxidation of NO with RO_2 ($\text{HO}_2 + \sum_i \text{R}_i\text{O}_2$) to form NO_2 that will rapidly form O_3 (R1-R2) (Bozem et al., 2017). For RO_2 we use the result from Eq. 3 that incorporates HO_2 and the sum of all further peroxy radicals $\sum_i \text{R}_i\text{O}_2$ (Parrish et al., 1986; Thornton et al., 2002).

$$P(\text{O}_3) = k_{\text{NO}+\text{HO}_2} \cdot [\text{NO}][\text{RO}_2] \quad (4)$$

Photochemical O_3 loss is mainly due to photolysis ($\lambda < 340$ nm) in the presence of water vapour and the reactions of ozone with OH and HO_2 (Bozem et al., 2017).



α , the fraction of $\text{O}(1\text{D})$ that reacts with H_2O

$$\alpha = \frac{k_{\text{O}(1\text{D})+\text{H}_2\text{O}}[\text{H}_2\text{O}]}{k_{\text{O}(1\text{D})+\text{H}_2\text{O}}[\text{H}_2\text{O}] + k_{\text{O}(1\text{D})+\text{M}}[\text{M}]} \quad (5)$$

was $(10.6 \pm 2.2) \%$ during AQABA with a quasi linear dependence on water concentrations. Furthermore, ozone is lost due to reactions with alkenes (R12) and halogen radicals (R13).



We find that the loss rate is dominated by the photolysis of ozone with subsequent reaction of $\text{O}(^1\text{D})$ with H_2O , was 60 – 80 % of the total loss rate, followed by the reaction of O_3 with HO_2 , which makes up 10 – 30 % (note that the uncertainty in HO_2 radical concentrations mentioned above has no significant influence on the total O_3 loss rate, due to its small contribution). The remaining fraction (10-30 %) is due to the reaction of O_3 with OH . The reaction of ozone with ethene is
 280 on average $0.005 - 0.01 \text{ ppb}_v \text{ h}^{-1}$ and therefore generally less than 2 % of the total ozone loss rate (Bourtsoukidis et al., 2019). The reaction of O_3 with all alkenes will hence be neglected. Halogen radicals were not measured during AQABA and will not be incorporated into our study. Therefore the noon-time chemical ozone loss rate can be summarized by

$$L(\text{O}_3) = [\text{O}_3] \cdot (\alpha \cdot j(\text{O1D}) + k_{\text{OH}+\text{O}_3} \cdot [\text{OH}] + k_{\text{HO}_2+\text{O}_3} [\text{HO}_2]). \quad (6)$$

NOPR presented in this study is finally calculated as the difference of Eq. 4 and Eq. 6.

$$285 \quad \text{NOPR} = k_{\text{NO}+\text{RO}_2} [\text{NO}][\text{RO}_2] - [\text{O}_3] \cdot (\alpha \cdot j(\text{O1D}) + k_{\text{OH}+\text{O}_3} [\text{OH}] + k_{\text{HO}_2+\text{O}_3} [\text{HO}_2]). \quad (7)$$

Under the assumption of constant chemical composition for a given day, the NOPR is expected to have a diel cycle following the measured actinic flux. Hence integrating the estimated NOPR over the course of a day based on the particular fractional noontime integral of $j(\text{NO}_2)$ will yield a diurnal value for NOPR. A detailed calculation of the diurnal fractional integrals is given in the supplements Figure S1. Note that all reaction rate constants used are from the IUPAC Task Force on
 290 Atmospheric Chemistry Chemical Kinetic Data Evaluation (Atkinson et al., 2004). Indications whether a chemical regime is NO_x -limited or VOC-limited can be derived from the ratio of HCHO to NO_2 . Former studies have derived HCHO/NO_2 -ratios from satellite measurements to establish whether ozone production is NO_x -limited or VOCs-limited. The results indicate NO_x -limitation for $\text{HCHO}/\text{NO}_2 > 2$ and prevailing VOC-limitation for $\text{HCHO}/\text{NO}_2 < 1$ (Duncan et al., 2010).

2.5 ECHAM/MESSy Atmospheric Chemistry (EMAC) model

295 EMAC is a 3D general circulation model that includes a variety of sub-models to describe numerous processes in the troposphere, their interaction with oceans and land surfaces and incorporates anthropogenic influences. Here we use the second development cycle of the Modular Earth Submodel System (MESSy2) (Jöckel et al., 2010) and ECHAM5 (Röckner et al., 2006) which is the fifth generation European Centre Hamburg general circulation model in the T106L31 resolution (corresponding to a quadratic grid of roughly 1.1° and 1.1°). The model has 31 vertical pressure levels and involves the
 300 complex organic chemistry mechanism MOM (Mainz Organic Mechanism) as presented by Sander et al. (2019) that includes further developments of the version used by Lelieveld et al. (2016b). Here we use the lowest pressure level in a terrain following coordinates (equivalent to the surface level) and simulations of NO , NO_2 , O_3 , OH , HO_2 , $j(\text{NO}_2)$ and $j(\text{O}^1\text{D})$.



The sum of peroxy radicals was estimated as the sum of all radicals R_iO_2 with less than 4 carbon atoms. Net ozone production based on data retrieved from EMAC was estimated as

$$305 \quad \text{NOPR} = [\text{NO}] \cdot (k_{\text{NO}+\text{HO}_2}[\text{HO}_2] + \sum_i k_{\text{NO}+R_iO_2}[R_iO_2]) - [\text{O}_3] \cdot (\alpha \cdot j(\text{O1D}) + k_{\text{OH}+\text{O}_3}[\text{OH}] + k_{\text{HO}_2+\text{O}_3}[\text{HO}_2]). \quad (8)$$

A list of all included peroxy radicals R_iO_2 for the reaction with NO is given in the supplementary Table ST9.

3 Results and discussions

3.1 NO_x and O_3 in the MBL around the Arabian Peninsula

During AQABA NO_x mixing ratios varied over five orders of magnitude with lowest values of less than 50 ppt_v observed in
 310 relatively pristine regions and highest values of several hundred ppb_v found in the vicinity of megacities or nearby passing
 ships. Ozone mixing ratios ranged from values of less than 20 ppb_v, detected over the Arabian Sea, to more than 150 ppb_v
 during episodes of severe pollution. Figures 3a) and 3b) show distributions of NO_x measured during the first and second leg
 of the campaign (range from 0.1 ppb_v to 20 ppb_v) while Figure 3c) and 3d) show corresponding ozone mixing ratios covering
 a range from 20 ppb_v to 100 ppb_v, respectively. A classification of the different regions based on Box-Whisker-Plots,
 315 including the 25-75-percentile interval (box) and whiskers for the 10-90-percentile interval, is shown in Figure 4 and Figure
 5 for NO_x and O_3 , respectively. As average NO_x is often influenced by fresh, localized emissions, we have included the
 median (black bar) instead of the average in the Box-Whisker-Plot for NO_x , which is less sensitive to extreme values. For O_3 ,
 although the difference between median and mean is mostly negligible, we also use the median in Figure 5. NO_x and O_3
 averages, medians, standard deviations, 1st and 3rd quantiles and the number of data points quantified per region are given in
 320 the supplementary Table ST2. See supplementary Figure S4 for OH and HO_2 mixing ratios around the Arabian Peninsula.

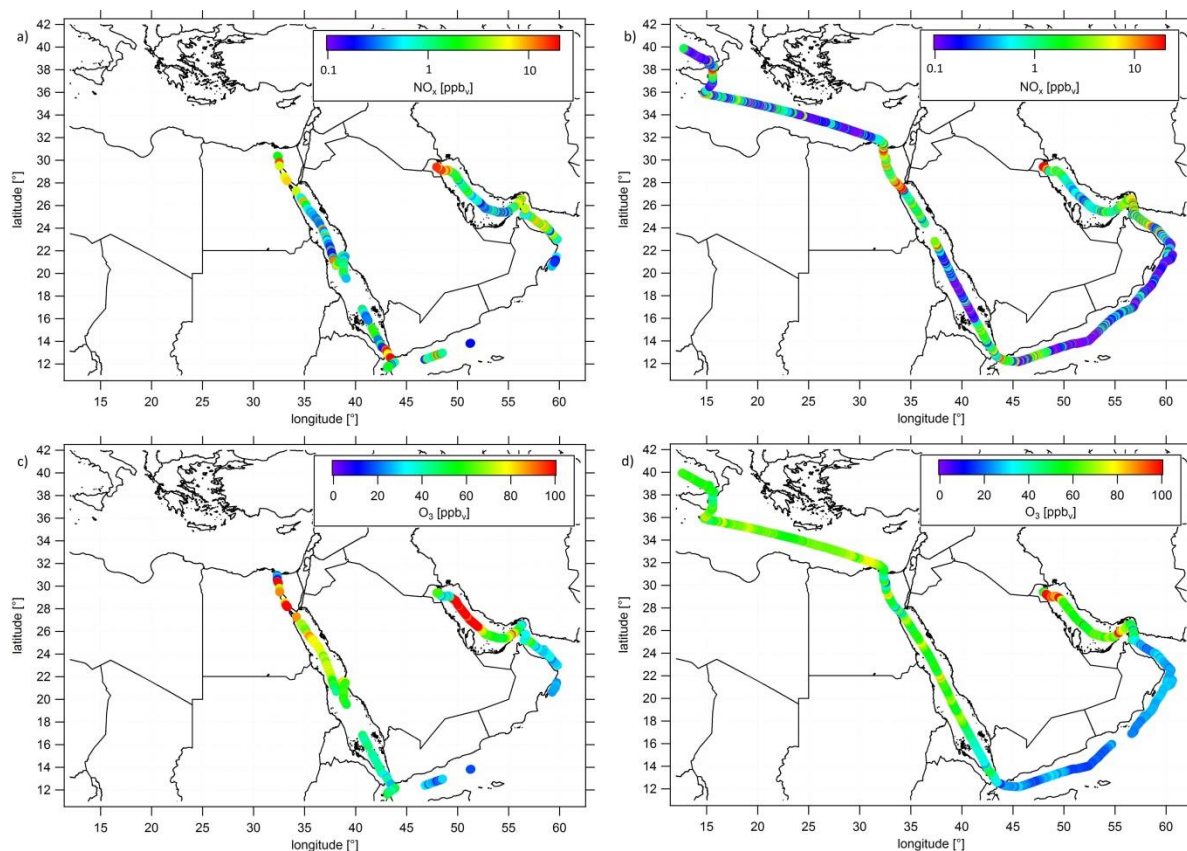
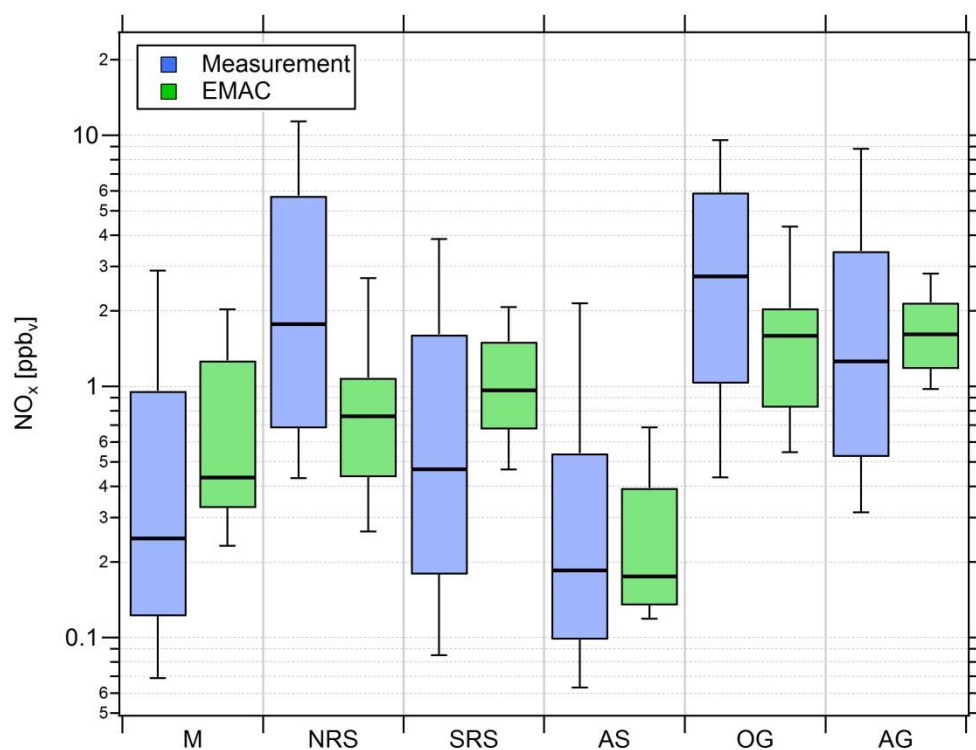
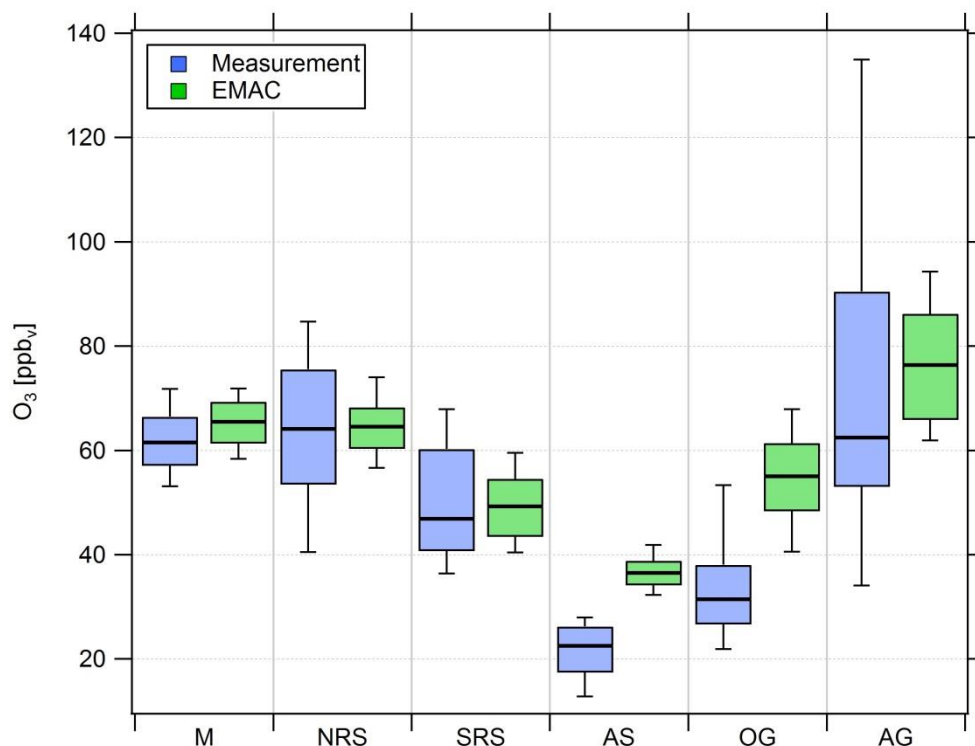


Figure 3: Ship cruises with color-scaled NO_x mixing ratios (logarithmic scale) a) during the first and b) the second leg and color-scaled O_3 mixing ratios (linear scale) c) during the first and d) during the second leg. Note that both NO_x and O_3 has been filtered for own stack contamination.



325

Figure 4: Comparison of measured (blue) and simulated (green) NO_x mixing ratios in the six different regions investigated during AQABA. The horizontal black bar indicates the median value, the box the 25- and 75-percentiles and the whiskers the 10- and 90-percentiles.



330 **Figure 5: Comparison of measured (blue) and simulated (green) O₃ mixing ratios in the six different regions investigated during AQABA. The horizontal black bar indicates the median value, the box the 25- and 75-percentiles and the whiskers the 10- and 90-percentiles.**

Overall, we find that NO_x mixing ratios over the Northern Red Sea, the Gulf of Oman and the Arabian Gulf are approximately one order of magnitude higher than in the other three regions (Southern Red Sea, Arabian Sea, Mediterranean). NO_x medians over the Arabian Gulf, the Northern Red Sea and the Gulf of Oman are 1.26 ppb_v, 1.76 ppb_v and 2.74 ppb_v, respectively. Lower median NO_x mixing ratios were measured over the Southern Red Sea (0.46 ppb_v), the Mediterranean (0.25 ppb_v) and the Arabian Sea (0.19 ppb_v). With respect to observed O₃ mixing ratios, the Arabian Sea is the only region representing remote MBL conditions with lowest median and average O₃ of 21.5 ppb_v and 22.5 ppb_v respectively, followed by the Gulf of Oman where median and mean O₃ were 31.5 ppb_v and 34 ppb_v, respectively. The low O₃ mixing ratios over the Arabian Sea were accompanied by the smallest variability (whisker-interval: 15.1 ppb_v). However, a significantly larger whisker-interval of 31.4 ppb_v over the Gulf of Oman indicates increasing amounts of pollution and advection from the Arabian Gulf where extreme events of ozone were observed several times during the campaign with maximum mixing ratios of up to 170 ppb_v. The whisker-interval over the Arabian Gulf was 100.9 ppb_v, more than six times higher than that over the Arabian Sea. Over the Mediterranean, the Northern Red Sea and the Southern Red Sea, median ozone was 61.5 ppb_v, 64.2 ppb_v and 46.9 ppb_v, respectively. The whisker-intervals over the Northern Red Sea and the Southern Red Sea were 44.2 ppb_v and 31.6 ppb_v, respectively. Photochemically aged air masses over the Mediterranean lead



to a rather small whisker-interval of 18.7 ppb_v. In summary, median NO_x over the Oman Gulf was 56 % and 117 % higher than over the Northern Red Sea and the Arabian Gulf, respectively. However, the highest NO_x average was measured over
350 the Northern Red Sea at 4.69 ppb_v, similar to the values observed over the Oman Gulf (4.16 ppb_v) and the Arabian Gulf (3.65 ppb_v). Note that highest NO_x mixing ratios over the Oman Gulf and over the Northern Red Sea are not always associated with high O₃ mixing ratios. We find that average ozone was highest over the Arabian Gulf with 74 ppb_v followed by the Northern Red Sea region (63.4 ppb_v). The average ozone mixing ratio over the Oman Gulf was 34 ppb_v, which corresponds to 46 % of the value observed over the Arabian Gulf. Photochemically aged air masses over the Mediterranean
355 Basin show an ozone average of 61.6 ppb_v and air masses encountered over the Northern Red Sea (O₃ median of 64.2 ppb_v, O₃ average of 63.4 ppb_v) are comparable to the Arabian Gulf.

Due to a number of large pollution sources in the region around the Arabian Peninsula such as passing ships, highly urbanized areas as well as on- and off-shore petrochemical processing, NO_x levels were rarely as low as those found in remote locations such as over the South Atlantic (Fischer et al., 2015) where NO_x levels may be under 20 ppt_v. Apart for a
360 few occasions where NO_x was below 50 ppt_v for short periods (Arabian Sea, the Southern Red Sea and the Mediterranean), NO_x levels during AQABA generally ranged from 100 ppt_v up to several ppb_v. The campaign NO_x median of 0.65 ppb_v and mean value of (2.51 ± 5.84) ppb_v is comparable to urban sites (Kleinman et al., 2005). A detailed emission density analysis performed by Johansson et al. (2017) shows that NO_x emissions in and around the Arabian Peninsula are amongst the highest worldwide, which could explain the rather high NO_x level in the MBL around the peninsula (Johansson et al., 2017;
365 Pfannerstill et al., 2019). O₃ mixing ratios measured during AQABA were also very variable with O₃ mixing ratios ranging between less than 20 ppb_v in the remote MBL (Fischer et al., 2015) to 60-70 ppb_v in the Mediterranean (consistent with previous ship-based measurements in the region (Velchev et al., 2011) and as high as 150 ppb_v measured over the Arabian Gulf region. The latter are consistent with O₃ mixing ratios reported from regions influenced by oil and gas processing (Edwards et al., 2014; Pfannerstill et al., 2019) and narrow shipping lanes such as the Houston Ship Channel (Kleinman et
370 al., 2005; Zhou et al., 2014).

Figure 4 also shows that the general trend for NO_x mixing ratios in the different regions is widely reproduced by the EMAC model. We find that the median NO_x(model)/NO_x(measurement)-ratio throughout the whole campaign is 0.91, indicating that the model underestimates NO_x by roughly 10 %. The average ratio and its standard deviation are significantly larger at 2.57 and 5.71, respectively, indicating that single modeled data points strongly exceed the measurements, especially during
375 periods of low in situ NO_x (see supplementary Figure S5). Particularly over the Arabian Sea and the Southern Red Sea, the model generally simulates NO_x mixing ratios higher than 100 and 200 ppt_v, respectively while the measurements indicate mixing ratios of less than 50 ppt_v for certain periods. Furthermore, as expected, the model is not able to reproduce point sources such as passing ships for which we observe a significant underestimation of the measured NO_x. For ozone we find that the median O₃(model)/O₃(measurement)-ratio throughout the campaign is 1.23, indicating that over the course of the



380 campaign the model overestimates O_3 by about 23 %. This could partly be related to the same limitation, i.e. the inability of
the model to resolve point sources in which O_3 is locally reduced due to titration by NO. While the model is in rather good
agreement with the measurements over the Mediterranean, the Northern Red Sea and Southern Red Sea, large deviations are
found over the Arabian Sea and the Oman Gulf, where the model overestimation with respect to the regional median is 63 %
and 75 %, respectively. A possible explanation for the overestimation of both ozone and NO_x in pristine regions such as over
385 the Arabian Sea and the Oman Gulf could be related to the model resolution of $1.1^\circ \times 1.1^\circ$. Interpolation of model
simulations along the *Kommandor Iona* ship track close to the coast at this resolution will most likely incorporate
contributions from nearby land areas, affected by anthropogenic emissions. See supplementary Table ST2 and Table ST3 for
further information and Figure S5 and S6 for additional scatterplots of measured and simulated regional median NO_x and O_3 ,
respectively.

390 3.2 Estimation of RO_2 around the Arabian Peninsula

Noontime RO_2 was estimated based on Eq. 3. As the steady state assumption will not hold for air masses originating from
fresh emissions (times to acquire steady state estimated from the inverse sum of the loss and production terms for NO_2
typically ranged from 1-2 minutes during AQABA) and for fast changes in the actinic flux, we have calculated Box-
Whisker-Plots for ± 2 h around noontime for which we expect relatively minor changes in the actinic flux (Fig. 6). The
395 noontime of each day was approximated by applying a Gaussian fit routine to the measured $j(NO_2)$ values whereas $j(NO_2)$
values being less than $10^{-3} s^{-1}$ were neglected. Due to the availability of OH and HO_2 data from July 18th 2017 onwards, we
have limited the analysis to this period. Note that there are no noontime RO_2 estimates from July 18th to July 21st due to
contamination by the ship exhaust and on August 24th 2017 due to missing data. The black bar in Fig. 6 indicates the median
value, with the Box-interval marking the 25- and 75-percentile and the whisker showing the 10- and 90-percentile. Figure 7
400 shows summarized regional trends of the RO_2 estimates for measured and simulated data.

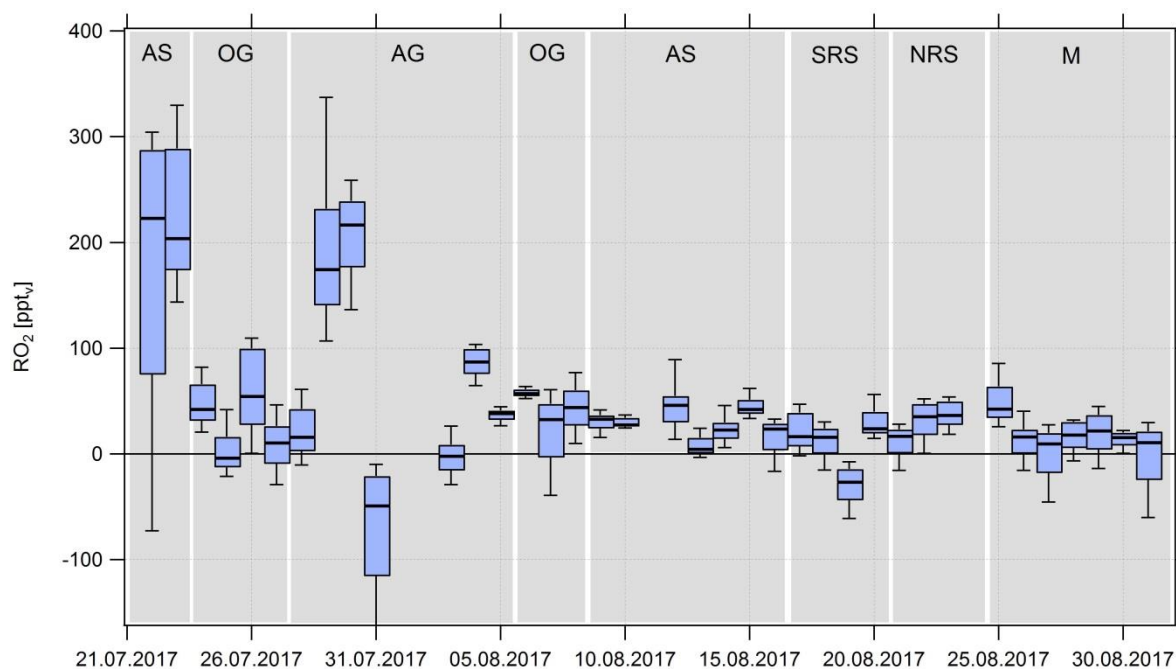


Figure 6: Timeline of median RO_2 noontime estimates from July 22nd to August 31st 2017. Due to contamination by the ship exhaust itself, there is no data from the July 18th to July 21st 2017. See annotations for the classification of the different regions.

405

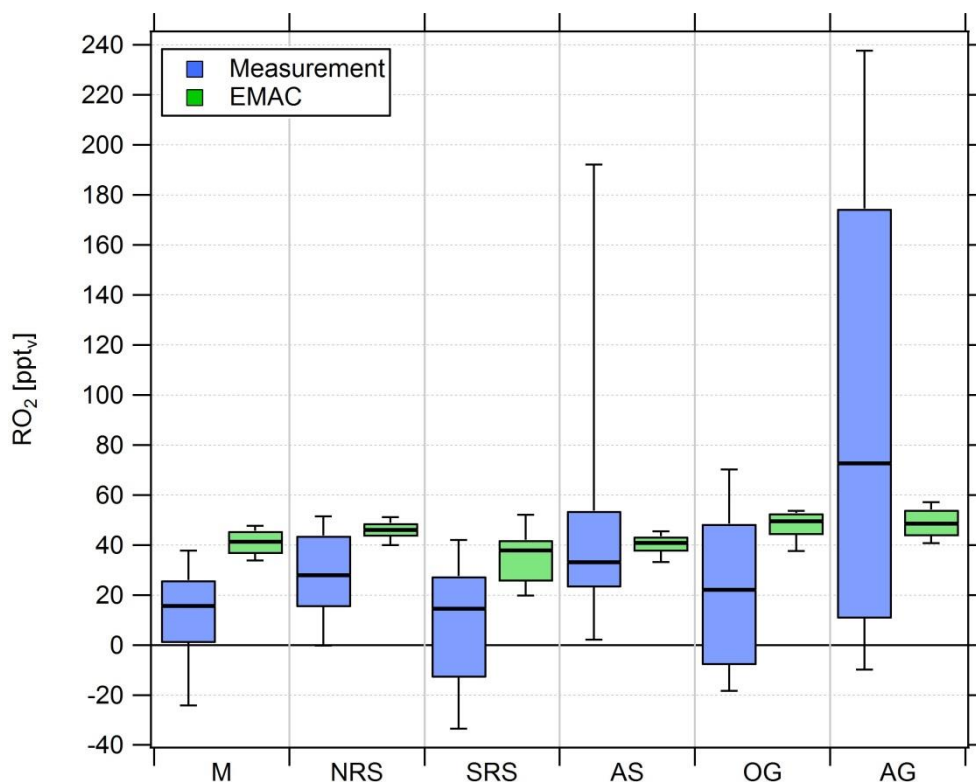


Figure 7: Comparison of Box-Whisker-Plots of the regional estimated noontime RO_2 median based on estimated and simulated data for the period from July 18th 2017 onwards.

410 We find median noontime RO_2 mixing ratios over the Mediterranean, the Northern Red Sea, the Southern Red Sea, the Arabian Sea and Oman Gulf of 16 ppt_v, 28 ppt_v, 15 ppt_v, 33 ppt_v and 22 ppt_v, respectively, with each respective 75-percentile RO_2 being equal or less than 54 ppt_v. Based on the total measurement uncertainties of the measured quantities in Eq. 3, the uncertainty in the RO_2 estimates is estimated at 14 %. Only over the Arabian Gulf, the RO_2 estimate yields a median noontime mixing ratio of 73 ppt_v accompanied by the largest variations in the box-interval of the whole campaign. While the

415 box-interval of the RO_2 estimate in the other regions is 25-57 ppt_v, the box-interval over the Arabian Gulf is significantly higher at 165 ppt_v. Negative values for all regions are regularly found in the vicinity of fresh emissions and air masses not in photochemical equilibrium. The elevated 90-percentile over the Arabian Sea is due to high RO_2 estimates during the first leg on July 22nd and 23rd.

Estimated RO_2 mixing ratios based on measured tracer data are in general agreement with previous studies performed in

420 marine boundary layer environments which report maximum mixing ratios between 30 and 55 ppt_v around noontime (Hernandez et al., 2001). As peroxy radicals are short-lived molecules generated from the oxidation of VOCs, enhanced RO_2

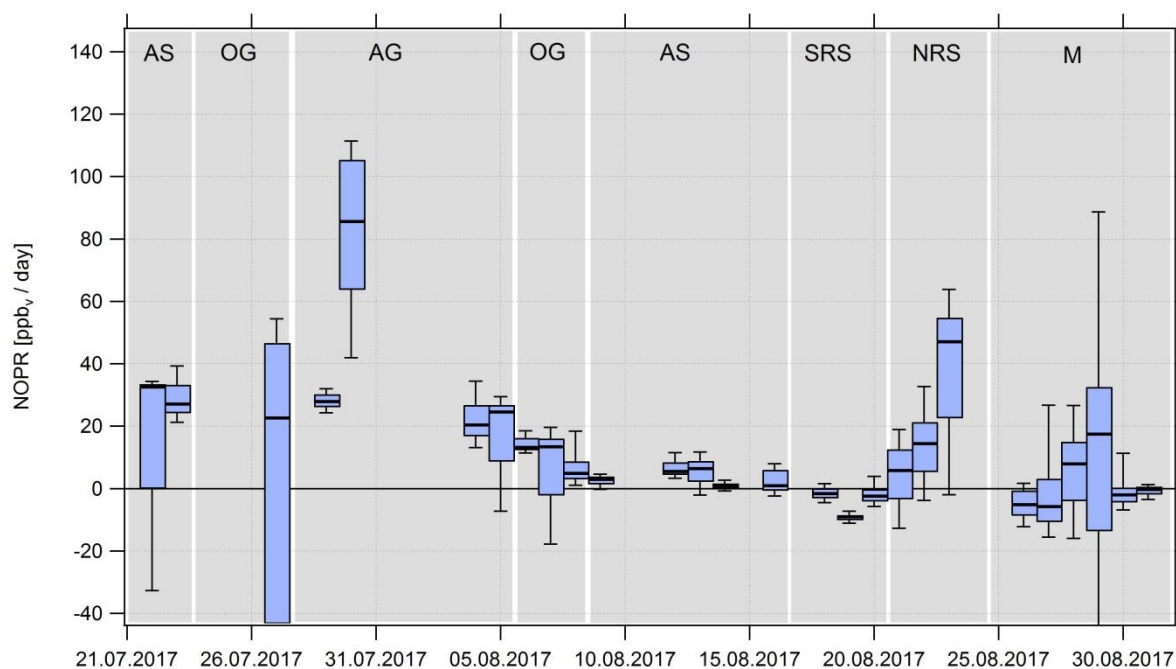


concentrations observed over the Arabian Gulf are most likely due to high VOC emissions from intense oil and gas activities in the region (Bourtsoukidis et al., 2019; Pfannerstill et al., 2019). Bourtsoukidis et al. report that spatial volume mixing ratios of ethane and propane over the Arabian Gulf were about a factor of 10-15 times higher than over the Arabian Sea and the Southern Red Sea (Bourtsoukidis et al., 2019). We find that the median noontime $\text{RO}_2(\text{estimated})/\text{HO}_2(\text{measurement})$ -ratio throughout the whole campaign is 1.54, indicating that throughout the campaign about one third of the sum of all peroxy radicals was represented by organic peroxy radicals. Note that during single days, HO_2 may be higher than the RO_2 estimate, which is within the uncertainty of the RO_2 estimate.

EMAC modelled, median noontime RO_2 mixing ratios estimated as the sum of simulated HO_2 and all simulated peroxy radicals with less than four carbon molecules are 41 ppt_v, 46 ppt_v, 38 ppt_v, 41 ppt_v, 50 ppt_v and 49 ppt_v over the Mediterranean, the Northern Red Sea, the Southern Red Sea, the Arabian Sea, the Oman Gulf and the Arabian Gulf, respectively. The observation based RO_2 estimate yields 16 ppt_v, 28 ppt_v, 15 ppt_v, 33 ppt_v, 22 ppt_v and 73 ppt_v, respectively. We find that the median point by point $\text{RO}_2(\text{model})/\text{RO}_2(\text{measurement})$ -ratio from July 18th onward is 1.05 so that, on average, the model overestimates the measurement by 5 %. Please note that the observational variability is much higher than the modeled one and that the median of 1.05 is accompanied by a larger average (1.84) and a large variability (42.51). See supplementary Table ST4 and ST5 for further information and Figure S7 for an additional scatterplot of measured and simulated regional median RO_2 .

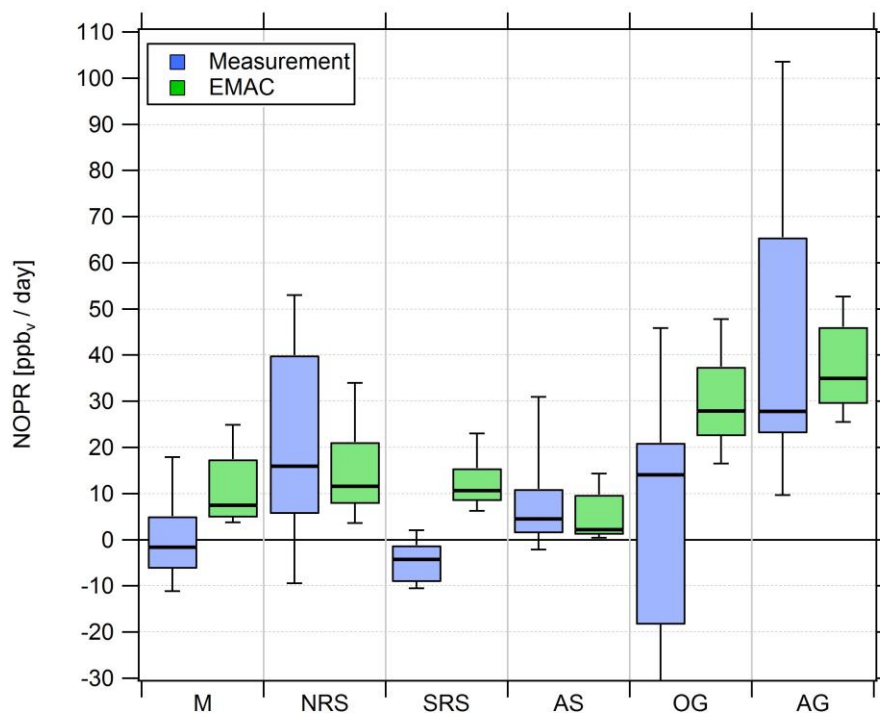
3.3 Net ozone production rates around the Arabian Peninsula

In the following, net ozone production rates (at noon) are calculated based on Eq. 7 for the different regions. These noontime values are then scaled to diurnal production rates (Fig. 8) based the integrated actinic flux as photochemical net ozone production is in good approximation linear with actinic flux. Due to contamination by the ship exhaust and due to the availability of OH and HO_2 data only from July 18th 2017 onwards, we have limited the analysis to the period from July 22nd 2017 to August 31st 2017. A comparison of NOPR estimated based on measured and simulated data for the different regions is shown in Fig. 9.



445

Figure 8: Timeline of the diurnal NOPR from July 22nd to August 31st 2017. NOPR calculations are limited to the time period from July 22nd onwards due to missing HO_x data and contamination before this period. See annotations for the classification of the different regions.



450



Figure 9: Diurnal net ozone production rates in the different regions. Related to the magnitude of pollution sources, the lower whisker of the NOPR estimate over the Oman Gulf is $-324 \text{ ppb day}^{-1}$.

Over the Mediterranean and the Southern Red Sea, NOPR values do not significantly deviate from zero (production equals
 455 loss) within the atmospheric variability (the uncertainty of the regional NOPR is 40 % which has been estimated by error
 propagation). However, the best estimate indicates slight net ozone destruction for the Mediterranean and Southern Red Sea
 (-2 ppb day^{-1}) and (-4 ppb day^{-1}) respectively, and slight net production for the Arabian Sea (5 ppb day^{-1}), which is
 significantly positive within the variability of the box-interval. Variations in NOPR calculated as the width of the 25-75-
 percentile-box yield comparable values of $9\text{--}11 \text{ ppb day}^{-1}$ for these three regions. Substantial net ozone production was
 460 inferred over the Oman Gulf, the Northern Red Sea, and the Arabian Gulf with the respective median values being 14 ppb
 day^{-1} , 16 ppb day^{-1} and 28 ppb day^{-1} , respectively. Especially over the Red Sea we find a strong latitudinal gradient in net
 ozone production rates with higher values towards the northern end, while slight net ozone destruction of -4 ppb day^{-1} is
 reported over the southern part.

NOPR estimates for the Oman Gulf, the Northern Red Sea and the Arabian Gulf are comparable to results reported for dense
 465 traffic shipping routes such as the Houston Ship Channel with NOPR of a few tens of ppb h^{-1} for periods of severe pollution
 (Zhou et al., 2014). Similar net ozone production rates have been reported for regions of Beijing in summer 2006 (Lu et al.,
 2010). For regions with low anthropogenic influence such as the Southern Red Sea and the Arabian Sea we estimate net
 ozone production that does not differ significantly from zero. This is due to the rather low NO_x mixing ratios in the clean
 marine boundary layer (Bozem et al., 2017). Note that we calculated net ozone destruction only for a few days over the
 470 Southern Red Sea and the Arabian Sea, indicating that the marine boundary layer around the Arabian Peninsula is rarely free
 from anthropogenic influence owing to the multitude of on- and off-shore anthropogenic activities.

We find that model-calculated estimates of NOPR reproduce the trends observed for NOPR calculated from in situ
 measurements except over the Mediterranean and the Southern Red Sea. Although EMAC predicts high ozone levels over
 the Arabian Sea, it also reports the lowest NOPR in this region. Deviations between model-calculated estimate and the
 475 estimate based on measured tracer data over the Mediterranean and over the Southern Red Sea could be linked to NO_x being
 overestimated in the model in these regions. As these regions have been classified as NO_x -limited ozone production regimes
 in this study, an increase in NO_x is expected to increase NOPR. In the model, pollution emissions, especially over the Oman
 Gulf and the Arabian Gulf, seem to be averaged over a large (1.1° grid size) region. High background concentrations of
 ozone precursors hence contribute to net ozone production rates that compare to conditions in highly polluted marine
 480 boundary air such as in the Houston Ship Channel (Zhou et al., 2014). Even in the more pristine regions such as over the
 Southern Red Sea and the Arabian Sea, the model is not able to reproduce net ozone destruction, which is consistent with the
 fact the ozone is generally too high and that NO_x levels below 0.1 ppbv are not found in the model. See supplementary Table
 ST6 and ST7 for further information and Figure S8 for an additional scatterplot of measured and simulated regional NOPR.



3.4 VOC and NO_x relationship to net ozone production

Ozone is photochemically formed when the precursors NO_x and VOCs are abundant in the presence of sunlight (Bozem et al., 2017; Jaffe et al., 2018). In order to determine whether a chemical system is NO_x- or VOC-limited or in a transition between those two regimes, one has to estimate the total amount of OH reactivity towards VOCs and towards NO_x. Therefore the VOC/NO_x-ratio is an important indicator of the behavior of NO_x, VOCs and O₃ in a system. Since it is not feasible to precisely define all ambient VOCs (could be thousands), formaldehyde mixing ratios have been used as a proxy for the OH reactivity towards VOCs since it is a short-lived oxidation product of many VOCs that is often positively correlated with peroxy radicals (Sillman et al., 1995; Duncan et al., 2010). Sillman et al. first used afternoon concentrations of indicator species such as HCHO and total reactive nitrogen (NO_y) to determine the sensitivity of ozone production to VOCs or NO_x (Sillman et al., 1995). Their approach was later successfully transferred to space-based satellite observations by using the ratio of tropospheric columns of HCHO and NO₂ to determine the sensitivity of ozone production (Martin et al., 2004). Here we use HCHO/NO₂-ratios (referred to as “Ratio”) deduced by Duncan et al. as indicators for the sensitivity of ozone production to NO_x- and VOC-limitations in megacities in the United States with large amounts of anthropogenic NO_x and VOC emissions (Duncan et al., 2010). The Ratio is an indicator of surface photochemistry as most of the atmospheric column of HCHO and NO₂ is located in the planetary boundary layer (Duncan et al., 2010). Duncan et al. have derived NO_x-limited ozone production regimes for HCHO/NO₂ > 2 and VOC-limited ozone production for HCHO/NO₂ < 1 (Duncan et al., 2010). For 1 < HCHO/NO₂ < 2 both NO_x and VOC emission reductions may lead to a reduction in ozone. Figure 10 shows the Box-Whisker-Plot classification of the HCHO/NO₂-ratio of the different regions during noontime.

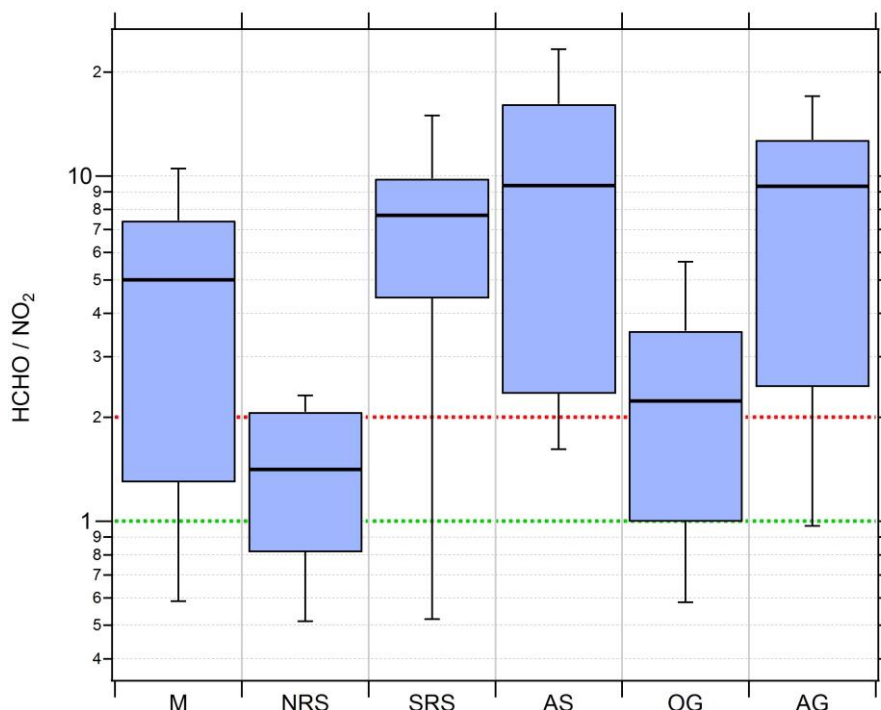


Figure 10: Box-Whisker-Plots of the HCHO/NO_2 -ratio for the different regions with the black bar indicating the median value. Red (ratio = 2) and green (ratio = 1) lines indicate the limits for HCHO/NO_2 deduced by Duncan et al. (2010) for NO_x -limitation and VOC-limitation, respectively.

Median HCHO/NO_2 -ratios of 5, 7.7, 9.4 and 9.3 over the Mediterranean, the Southern Red Sea, the Arabian Sea and the Arabian Gulf respectively indicate tendencies towards NO_x -limited regimes. In a previous study based on measured OH reactivity, Pfannerstill et al. classified these regions as being mostly in a transition between NO_x - and VOC-limitation, with a tendency towards NO_x -limitation (2019). Median HCHO/NO_2 -ratios of 1.4 and 2.2 estimated over the Northern Red Sea and the Oman Gulf signify tendencies towards VOC-limitation. However, none of the medians of the six regions falls below the VOC-limit deduced by Duncan et al. (2010).

Over the Red Sea we find a latitudinal gradient in the HCHO/NO_2 -ratio, similar to the gradients for NO_x and NOPR. Due to very low NO_x over the Southern Red Sea, O_3 production is NO_x -limited, changing into a more VOC-limited regime over the Northern Red Sea. Photochemical aging of the air over the Mediterranean leads to a NO_x -limited regime. NO_x limitation is also inferred for the relatively clean Arabian Sea and the polluted Arabian Gulf atmosphere. Note that a future increase in emissions of NO_x from increased shipping in the Arabian Gulf would thus lead to higher NOPR further increasing ozone pollution in the region (Johansson et al., 2017). See Table ST8 for detailed statistics on regional HCHO/NO_2 -ratios.



4 Conclusion

In situ observations of NO, NO₂, O₃, HCHO, OH, HO₂, absolute humidity, actinic flux, temperature and pressure were carried out in the marine boundary layer around the Arabian Peninsula during the AQABA ship campaign from late June to early September 2017. Concentration ranges of both NO_x and O₃ clearly showed anthropogenic influence in the MBL. NO_x was highest over the Arabian Gulf, the Northern Red Sea and the Oman Gulf. Lowest NO_x was observed over the Arabian Sea and over the Southern Red Sea during the second leg. O₃ mixing ratios were highest over the Arabian Gulf. We observed a latitudinal gradient in O₃ concentrations with higher values towards the northern part of the Red Sea. Although comparable O₃ averages were measured over the Northern Red Sea and over the Mediterranean, lower variability over the Mediterranean towards the end of August 2017 indicates photochemically more extensively aged air masses. The lowest regional O₃ mixing ratio average was detected over the Arabian Sea, which is broadly comparable to remote marine boundary layer conditions in the Northern Hemisphere.

Noontime RO₂ estimates based on deviations from the Leighton Ratio yield median values around the Arabian Peninsula amount to 15 – 33 ppt_v for all regions except over the Arabian Gulf where the median is 73 ppt_v. The uncertainty due to the missing up-welling actinic flux portion is expected to be insignificant. Furthermore, we estimated noontime and diurnal NOPR based on Eq. 6 and the integral over the actinic flux. Highest diurnal NOPR were observed over the Oman Gulf, the Northern Red Sea and the Arabian Gulf with median values of 14 ppb_v day⁻¹, 16 ppb_v day⁻¹ and 28 ppb_v day⁻¹, respectively, which is in agreement with previous studies that predicted net photochemical O₃ formation conditions in the region. Net ozone destruction was only observed for a few days with clean conditions over the Arabian Sea and the Southern Red Sea. Based on HCHO/NO₂-ratios our analysis suggests tendencies towards NO_x-limitation over the Mediterranean, the Southern Red Sea, the Arabian Sea and the Arabian Gulf and VOC-limitation over the Northern Red Sea and the Oman Gulf, which reproduces the trends observed by Pfannerstill et al. (2019).

NO_x results from the atmospheric chemistry – general circulation model EMAC underestimate the measurement data by 10 % whereas median modeled O₃ overestimates the measurement by 23 %, the latter being related to limitations in model resolution in coastal proximity and near shipping lanes. Although EMAC generally reproduces regional NO_x and O₃ medians, the scatter when comparing both data sets is large. NO_x is generally too low as it does not resolve local point sources and too high for clean regions. Lowest NO_x of less than 0.1 ppb_v found in the in situ measurements is not reproduced by the model as emissions are averaged over a large area (1.1°). Median noontime RO₂ retrieved from the EMAC model are ~ 5 % higher than RO₂ estimates based on measurement data, however, the RO₂ sum deduced from EMAC is sometimes about a factor of 2 higher than the regional RO₂ estimate based on the Leighton Ratio and measured tracer data. NOPR estimates based on modeled data reproduce the tendencies derived from the measurements very well. However, the model does not reproduce observed net ozone destruction along some clean parts of the ship cruise.



Data availability

Data used in this study is available to all scientists agreeing to the AQABA protocol at <https://doi.org/10.5281/zenodo.3531501>.

555 Author contributions

IT, HF and JL designed the study. UP and IT performed the CLD NO and NO₂ measurements and processed the data. JC and PE performed the O₃ measurements, JS performed the actinic flux measurements. JS performed cavity ring-down spectroscopy measurements of NO₂. DD and BH performed the HCHO measurements. HH, MM, RR, ST performed the OH and HO₂ measurements. J-DP was responsible for the H₂O measurements. Model simulations were made by AP. All authors
560 have contributed to writing this manuscript

Competing interests

The authors declare no conflict of interest.

Acknowledgements

We acknowledge the collaborations with King Abdullah University of Science and Technology (KAUST), The Cyprus
565 Institute (CyI) and the Kuwait Institute for Scientific Research (KISR). We would like to thank Marcel Dorf and Claus Koeppel for the organization of the campaign. We would like to thank Hays Ships Ltd. and the ship crew for caring about the physical well-being of the scientific participants and for an unforgettable time on board *Kommandor Iona*. Last but not least we would like to thank the whole AQABA community for a successful campaign.

570



Appendix: Acronyms and abbreviations

General

	AQABA	<u>A</u> ir <u>Q</u> uality and Climate in the <u>A</u> rabian <u>B</u> asin campaign
	CyI	The <u>C</u> yprus <u>I</u> nstitute
575	KAUST	<u>K</u> ing <u>A</u> bdullah <u>U</u> niversity of <u>S</u> cience and <u>T</u> echnology
	KISR	<u>K</u> uwait <u>I</u> nstitute for <u>S</u> cientific <u>R</u> esearch

Regions

	AG	<u>A</u> rabian <u>G</u> ulf
	AS	<u>A</u> rabian <u>S</u> ea
580	M	<u>M</u> editerranean Sea
	NRS	<u>N</u> orthern <u>R</u> ed <u>S</u> ea
	OG	<u>O</u> man <u>G</u> ulf
	SRS	<u>S</u> outhern <u>R</u> ed <u>S</u> ea

Scientific

585	CLD	<u>C</u> hemiluminescence <u>d</u> etector
	CRDS	<u>C</u> avity <u>r</u> ing- <u>d</u> own <u>s</u> pectroscopy
	ECHAM5	Fifth generation <u>E</u> uropean <u>C</u> entre <u>H</u> amburg general circulation model
	EMAC	<u>E</u> CHAM/ <u>M</u> ESSy <u>A</u> tmospheric <u>C</u> hemistry model
	FWHM	<u>F</u> ull <u>w</u> idth at <u>h</u> alf <u>m</u> aximum
590	GC-FID	<u>G</u> as <u>c</u> hromatography – <u>f</u> lame <u>i</u> onization <u>d</u> etector
	HORUS	<u>H</u> yd <u>r</u> <u>O</u> xyl <u>R</u> adical measurement <u>U</u> nit based on fluorescence <u>S</u> pectroscopy instrument
	HO _x	OH + HO ₂
	LED	<u>L</u> ight <u>e</u> mitting <u>d</u> iode
	LIF	<u>L</u> aser <u>i</u> nduced <u>f</u> luorescence
595	MBL	<u>M</u> arine <u>b</u> oundary <u>l</u> ayer
	MESSy	<u>M</u> odular <u>E</u> arth <u>S</u> ubmodel <u>S</u> ystem
	NOPR	<u>N</u> et <u>o</u> zone <u>p</u> roduction <u>r</u> ate
	NO _x	NO + NO ₂
	PFA	<u>P</u> er <u>f</u> luoroalkoxy
600	PSS	<u>P</u> hotostationary <u>s</u> teady <u>s</u> tate
	PTFE	<u>P</u> oly <u>t</u> etra <u>f</u> luoro <u>e</u> thylene
	SLM	<u>S</u> tandard <u>l</u> iter per <u>m</u> inute
	STEAM3	<u>S</u> hip <u>T</u> raffic <u>E</u> mission <u>A</u> ssessment <u>M</u> odel 3
	TMU	<u>T</u> otal <u>m</u> easurement <u>u</u> ncertainty
605	VOC	<u>V</u> olatile <u>o</u> rganic <u>c</u> ompounds
	UV	<u>U</u> ltraviolet



References

- Atkinson, R., Baulch, D. L., Cox, R. A., Crowley, J. N., Hampson, R. F., Hynes, R. G., Jenkin, M. E., Rossi, M. J., and Troe, J.: *Atmos. Chem. Phys.*, 4, 1461, 2004; IUPAC Task Group on Atmospheric Chemical Kinetic Data Evaluation, (<http://iupac.pole-ether.fr>).
- 615 Bourtsoukidis, E., Ernle, L., Crowley, J. N., Lelieveld, J., Paris, J.-D., Pozzer, A., Walter, D., and Williams, J.: Non Methane Hydrocarbon (C2-C8) sources and sinks around the Arabian Peninsula, doi:10.5194/acp-2019-92, 2019.
- Bozem, H., Butler, T.M., Lawrence, M. G., Harder, H., Martinez, M., Kubistin, D., Lelieveld, J., and Fischer, H.: Chemical processes related to net ozone tendencies in the free troposphere, *Atmos. Chem. Phys.*, 17, 10565-10582, doi:10.5194/acp-17-10565-2017, 2017.
- 620 Cantrell, C. A., Shetter, R. E., Calvert, J. G., Eisele, F. L., Williams, E., Baumann, K., William, H. B., Stevens, P. S., Mather, J., H.: Peroxy radicals from photostationary state deviations and steady state calculations during the Tropospheric OH Photochemistry Experiment at Idaho Hill, Colorado, 1993, *J. Geophys. Res.*, 102, 6369-6378, 1997.
- Celik, S., Drewnick, F., Fachinger, F., Brooks, J., Darbyshire, E., Paris, J.-D., Eger, P. G., Schuladen, J., Tadic, I., Friedrich, N., Dienhart, D., Crowley, J. N., Harder, H., and Borrmann, S.: Influence of vessel characteristics and atmospheric processes on the gas and particle phase of ship emission plumes measured in the Mediterranean Sea and around the Arabian Peninsula, *Atmos.-Chem. Phys. Discuss.*, <https://doi.org/10.5194/acp-2019-859>, in review, 2019.
- 625 Crutzen, P. J.: Photochemical reactions initiated by and influencing ozone in unpolluted tropospheric air, *Tellus*, 26, 47–57, doi:10.1111/j.2153-3490.1974.tb01951.x, 1973.
- Duncan, B. N., Yoshida, Y., Olson, J. R., Sillman, S., Martin, R. V., Lamsal, L., Hu, Y., Pickering, K. E., Retscher, C., Allen, D. J., Crawford, J. H.: Application of OMI observations to a space-based indicator of NO_x and VOC controls on surface ozone formation, *J. Atmos. Env.*, 44, 2213-2223, doi:10.1016/j.atmosenv.2010.03.010, 2010.
- 630 Drummond, J.W., Volz, A., and Ehhalt, D. H.: An optimized chemiluminescence detector for tropospheric NO measurements, *J. Atmos. Chem.*, 2, 287–306, doi:10.1007/BF00051078, 1985.
- Edwards, P. M., Brown, S. S., Roberts, J. M., Ahmadov, R., Banta, R. M., deGouw, J. A., Dubé, W. P., Field, R. A., Flynn, J. H., Gilman, J. B., Graus, M., Helmig, D., Koss, A., Langford, A. O., Lefer, B. L., Lerner, B. M., Li, R., Li, S.-M., McKeen, S. A., Murphy, S. M., Parrish, D. D., Senff, C. J., Soltis, J., Stutz, J., Sweeney, C., Thompson, C. R., Trainer, M. K., Tsai, C.,



- Veres, P. R., Washenfelder, R. A., Warneke, C., Wild, R. J., Young, C. J., Yuan, B., and Zamora, R.: High winter ozone pollution from carbonyl photolysis in an oil and gas basin, *Nature*, 514, 351-354, doi:10.1038/nature13767, 2014.
- Fischer, H., Pozzer, A., Schmitt, T., Jöckel, P., Klippel, T., Taraborrelli, D., and Lelieveld, J.: Hydrogen peroxide in the marine boundary layer over the South Atlantic during the OOMPH cruise in March 2007, *Atmos. Chem. Phys.*, 15, 6971-6980, doi:10.5194/acp-15-6971-2015, 2015.
- Hauglustaine, D. A., Madronich, S., Ridley, B. A., Walega, J. G., Cantrell, C. A., and Shetter, R. E.: Observed and model-calculated photostationary state at Mauna Loa Observatory during MLOPEX 2, *J. Geophys. Res.*, 101, 14681-14696, doi:10.1029/95JD03612, 1996.
- 645 Hens, K., Novelli, A., Martinez, M., Auld, J., Axinte, R., Bohn, B., Fischer, H., Keronen, P., Kubistin, D., Nölscher, A. C., Oswald, R., Paasonen, P., Petäjä, T., Regelin, E., Sander, R., Sinha, V., Sipilä, M., Taraborrelli, D., Tatum Ernest, C., Williams, J., Lelieveld, J., Harder, H.: Observation and modelling of HO_x radicals in a boreal forest, *Atmos. Chem. Phys.*, 14, 8723-8747, doi:10.5194/acp-14-8723-2014, 2014.
- Hernandez, M. D. A., Burkert, J., Reichert, L., Stöbener, D., Meyer-Arne, J., and Burrows, J. P.: Marine boundary layer peroxy radical chemistry during the AEROSOLS99 campaign: Measurements and analysis, *J. Geophys. Res.*, 106, 20833-20846, doi:10.1029/2001JD900113, 2001.
- 650 Hollaway, M. J., Arnold, S. R., Challinor, A. J., and Emberson, L. D.: Intercontinental trans-boundary contributions to ozone-induced crop yield losses in the Northern Hemisphere, *Biogeosciences*, 9, 271-292, doi:10.5194/bg-9-271-2012, 2012.
- Hosaynali Beygi, Z., Fischer, H., Harder, H. D., Martinez, M., Sander, R., Williams, J., Brookes, D. M., Monks, P. S., and Lelieveld, J.: Oxidation photochemistry in the Southern Atlantic boundary layer: unexpected deviations of photochemical steady state, *Atmos. Chem. Phys.*, 11, 8497-8513, doi:10.5194/acp-11-8497-2011, 2011.
- Jaffe, D. A., Cooper, O. R., Fiore, A. M., Henderson, B. H., Tonnesen, G. S., Russell, A. G., Henze, D. K., Langford, A. O., Lin, M., and Moore, T.: Scientific assessment of background ozone over the U.S.: Implications for air quality management, *Elem. Sci. Anth.*, 6, 56, doi:10.1525/elementa.309, 2018.
- 660 Javed, U., Kubistin, D., Martinez, M., Pollmann, J., Rudolf, M., Parchatka, U., Reiffs, A., Thieser, J., Schuster, G., Horbanski, M., Pöhler, D., Crowley, J. N., Fischer, H., Lelieveld, J., and Harder, H.: Laser-induced fluorescence-based detection of atmospheric nitrogen dioxide and comparison of different techniques during the PARADE 2011 field campaign, *Atmos. Meas. Tech.*, 12, 1461-1481, doi:10.5194/amt-12-1461-2019, 2019.



- Jöckel, P., Kerkweg A., Pozzer, A., Sander, R., Tost, H., Riede, H., Baumgartner, A., Gromov, S., and Kern, B.:
665 Development of cycle 2 of the Modular Earth Submodel System (MESSy2), *Geosci. Model Dev.*, 3, 717-752,
doi:10.5194/gmd-3-717-2010, 2010.
- Johansson, L., Jalkanen, J.-P., Kukkonen, J.: Global assessment of shipping emissions in 2015 on a high spatial a temporal
resolution, *J. Atmos. Env.*, 167,403-415, doi:10.1016/j.atmosenv.2017.08.042., 2017.
- Keller-Rudek, H., Moortgat, G. K., Sander, R., and Sörensen, R.: The MPI-Mainz UV/VIS Spectral Atlas of Gaseous
670 Molecules of Atmospheric Interest, *Earth Syst. Sci. Data*, 5, 365-373, doi:10.5194/essd-5-365-2013, 2013.
- Kleinman, L. I., Daum, P. H., Lee, Y.-N., Nunnermacker, L. J., Springston, S. R. Weinstein-Lloyd, J., and Rudolph, J.: A
comparative study of ozone production in five U.S. metropolitan areas, *J. Geophys. Res.-Atmos.*, 110, D02301,
doi:10.1029/2004jd005096, 2005.
- Klonecki, A. and Levy, H.: Tropospheric chemical ozone tendencies in CO-CH₄-NO_y-H₂O system: Their sensitivity to
675 variations in environmental parameters and their application to a global chemistry transport model study, *J. Geophys. Res.*,
102, 21221–21237, doi:10.1029/97JD01805, 1997.
- Kormann, R., Fischer, H., de Reus, M., Lawrence, M., Brühl, Ch., von Kuhlmann, R., Holzinger, R., Williams, J., Lelieveld,
J., Warneke, C., de Gouw, J., Heland, J., Ziereis, H., and Schlager, H.: Formaldehyde over the eastern Mediterranean during
MINOS: Comparison of airborne in-situ measurements with 3D-model results, *Atmos. Chem. Phys.*, 3, 851-861,
680 doi:10.5194/acp-3-851-2003, 2003.
- Krotkov, N. A., McLinden, C. A., Li, C., Lamsal, L. N., Celarier, E. A., Marchenko, S. V., Swartz, W. H., Bucsela, E. J.,
Joiner, J., Duncan, B. N., Boersma, K. F., Veefkind, J. P., Levelt, P. F., Fioletov, V. E., Dickerson, R. R., He, H., Lu, Z., and
Streets, D. G.: Aura OMI observations of regional SO₂ and NO₂ pollution changes from 2005 to 2015, *Atmos. Chem. Phys.*,
16, 4605–4629, doi:10.5194/acp-16-4605-2016, 2016.
- 685 Kwok, C. Y., Laurent, O., Guemri, A., Philippon, C., Wastine, B., Rella, C. W., Vuillemin, C., Truong, F., Delmotte, M.,
Kazan, V., Darding, M., Lebegue, B., Kaiser, C., Xueref-Remy, I., and Ramonet, M.: Comprehensive laboratory and field
testing of cavity ring-down spectroscopy analyzers measuring H₂O, CO₂, CH₄ and CO, *Atmos. Chem. Phys.*, 8, 3867-3892,
doi:10.5194/amt-8-3867-2015, 2015.
- Leighton, P. A.: Photochemistry of air pollution, *Phys. Chem.*, 9, 1961.



- 690 Lelieveld, J., Dentener, F. J., Peters, W., and Krol, M. C.: On the role of hydroxyl radicals in the self-cleansing capacity of the troposphere, *Atmos. Chem. Phys.*, 4, 2337–2344, doi:10.5194/acp-4-2337-2004, 2004.
- Lelieveld, J., Hoor, P., Jöckel, P., Pozzer, A., Hadjinicolaou, P., Cammas, J.-P., and Beirle, S.: Severe ozone air pollution in the Persian Gulf region, *Atmos. Chem. Phys.*, 9, 1393–1406, doi:10.5194/acp-9-1393-2009, 2009.
- Lelieveld, J.: Strongly increasing heat extremes in the Middle East and North Africa (MENA) in the 21st century, *Climate Change*, 137, 245–260, doi:10.1007/s10584-016-1665-6, 2016a.
- 695 Lelieveld, J., Gromov, S., Pozzer, A., and Taraborrelli, D.: Global tropospheric hydroxyl distribution, budget and reactivity, *Atmos. Chem. Phys.*, 16, 12477–12493, doi:10.5194/acp-16-12477-2016, 2016b.
- Liu, F., Beirle, S., Zhang, Q., Dörner, S., He, K., and Wagner, T.: NO_x lifetimes and emissions of cities and power plants in polluted background estimated by satellite observations, *Atmos. Chem. Phys.*, 16, 5823–5298, doi:10.5194/acp-16-5283-2016, 2016.
- 700 Lu, K., Zhang, Y., Su, H., Brauers, T., Chou, C., Hofzumahaus, A., Liu, S., Kita, K., Kondo, K., Shao, M., Wahner, A., Wang, J., Wang, X., and Zhu, T.: Oxidant (O₃+NO₂) production processes and formation in regimes in Beijing, *J. Geophys. Res.*, 115, D07303, doi:10.1029/2009JD012714, 2010.
- Mallik, C., Tomsche, L., Bourtsoukidis, E., Crowley, J. N., Derstroff, B., Fischer, H., Hafermann, S., Hüser, I., Javed, U., Keßel, S., Lelieveld, J., Martinez, M., Meusel, H., Novelli, A., Phillips, G. J., Pozzer, A., Reiffs, A., Sander, R., Taraborrelli, D., Sauvage, C., Schuladen, J., Su, H., Williams, J., and Harder, H.: Oxidation processes in the eastern Mediterranean atmosphere: evidence from the modelling of HO_x measurements over Cyprus, *Atmos. Chem. Phys.*, 18, 10825–10847, doi:10.5194/acp-18-10825-2018, 2018.
- Mannschreck, K., Gilge, S., Plass-Duelmer, C., Fricke, W., and Berresheim, H.: Assessment of the applicability of NO-NO₂-O₃ photostationary state to long-term measurements at the Hohenpeissenberg GAW Station, Germany, *Atmos. Chem. Phys.*, 4, 1265–1277, doi:10.5194/acp-4-1265-2004, 2004.
- 710 Martin R., Fiore, A., Van Donkelaar, A. 2004: Space-based diagnosis of surface ozone sensitivity to anthropogenic emissions, *Geophys. Res. Lett.*, 31, L06120, doi:10.1029/2004GL019416, 2004.
- Martinez, M., Harder, H., Kubistin, D., Rudolf, M., Bozem, H., Eerdekens, G., Fischer, H., Klüpfel, T., Gurk, C., Königstedt, R., Parchatka, U., Schiller, C. L., Stickler, A., Williams, J., and Lelieveld, J.: Hydroxyl radicals in the tropical



- troposphere over the Suriname rainforest: airborne measurements, *Atmos. Chem. Phys.*, 10, 3759-3773, doi: 10.5194/acp-10-3759-2010, 2010.
- Meusel, H., Kuhn, U., Reiffs, A., Mallik, C., Harder, H., Martinez, M., Schuladen, J., Bohn, B., Parchatka, U., Crowley, J. N., Fischer, H., Tomsche, L., Novelli, A., Hoffmann, T., Janssen, R. H. H., Hartogensis, O., Pikridas, M., Vrekoussis, M.,
720 Bourtsoukidis, E., Weber, B., Lelieveld, J., Williams, J., Pöschl, U., Cheng, Y., and Su, H.: Daytime formation of nitrous acid at a coastal remote site in Cyprus indicating a common ground source of atmospheric HONO and NO, *Atmos. Chem. Phys.*, 16, 14475-14493, doi:10.5194/acp-16-14475-2016, 2016.
- Miyazaki, K., Eskes, H., Sudo, K., Folkert Boersma, K., Bowman, K., and Kanaya, Y.: Decadal changes in global surface NO_x emissions from multi-constituent satellite data assimilation, *Atmos. Chem. Phys.*, 17, 807-837, doi:10.5194/acp-17-
725 807-2017, 2017.
- Monks, P. S., Archibald, A. T., Colette, A., Cooper, O. Coyle, M., Derwent, R., Fowler, D., Granier, C., Law, K. S., Mills, G. E., Stevenson, D. S., Tarasova, O., Thouret, V., von Schneidemesser, E., Sommariva, R., Wild, O., Williams, M. L.: Tropospheric ozone and its precursors from the urban to the global scale from air quality to short-lived climate forcer, *Atmos. Chem. Phys.*, 15, 8889-8973, doi:10.5194/acp-15-8889-2015, 2015.
- 730 Nakamura, K., Kondo, Y., Chen, G., Crawford, J. H., Takegawa, N., Koike, M., Kita, K., Miyazaki, Y., Shetter, R. E., Lefer, B. L., Avery, M., and Matsumoto J.: Measurement of NO₂ by the photolysis conversion technique during the Transport and Chemical Evolution Over the Pacific (TRACE-P) campaign, *J. Geophys. Res.*, 108, D24, 4752, doi:10.1029/2003JD003712, 2003.
- Parrish, D. D., Trainer, M., Williams, E. J., Fahey D. W., Hübler, G., Eubank, C. S., Liu S. C., Murphy, P. C., Albritton, D.
735 L., Fehsenfeld, F. C.: Measurements of the NO_x-O₃-photostationary steady state at Niwot Ridge, Colorado, *J. Geophys. Res.*, 91, 5361-5370, doi:10.1029/JD091iD05p05361, 1986.
- Pollack, I. B., Lerner, B. M., Ryerson, T. B.: Evaluation of ultraviolet light-emitting diodes for detection of atmospheric NO₂ by photolysis – chemiluminescence, *J. Atmos. Chem.*, 65, 111-125, doi:10.1007/s10874-011-9184-3, 2011.
- Pfannerstill, E. Y., Wang, N., Edtbauer, A., Bourtsoukidis, E., Crowley, J. N., Dienhart, D., Eger, P. G., Ernle, L., Fischer, H., Hottmann, B., Paris, J.-D., Stönnner, C., Tadic, I., Walter, D., Lelieveld, J., Williams, J.: Shipborne measurements of total OH reactivity around the Arabian Peninsula and its role in ozone chemistry, *Atmos. Chem. Phys.*, 19, 11501-11523, doi:10.5194/acp-19-11501-2019, 2019.



Reed, C., Evans, M. J., Di Carlo, P., Lee, J. D., and Carpenter, L. J.: Interferences in photolytic NO₂ measurements: explanation for an apparent missing oxidant?, *Atmos. Chem. Phys.*, 16, 4707–4724, doi:10.5194/acp-16-4707-2016, 2016.

- 745 Regelin, E., Harder, H., Martinez, M., Kubistin, D., Tatum Ernest, C., Bozem, H., Klippel, T., Hosaynali Beygi, Z., Fischer, H., Sander, R., Jöckel, P., Königstedt, R., and Lelieveld, J.: HO_x measurements in the summertime upper troposphere over Europe: a comparison of observations to a box model and a 3-D model, *Atmos. Chem. Phys. Phys.*, 13, 10703–10720, doi:10.5194/acp-13-10703-2013, 2013.

- Roeckner, E., Brokopf, R., Esch, M., Giorgetta, M., Hagemann, S., Kornblueh, L., Manzini, E., Schlese, U., and
750 Schulzweida, U.: Sensitivity of Simulated Climate to Horizontal and Vertical Resolution in the ECHAM5 Atmosphere Model, *J. Climate*, 19, 3771–3791, doi:10.1175/JCLI3824.1, 2006.

Ryerson, T. B., Williams, E. J., and Fehsenfeld, F. C.: An efficient photolysis system for fast-response NO₂ measurements, *J. Geophys. Res.*, 105, D21, 26447–26461, doi:10.1029/2000JD900389, 2000.

- Sander, R., Baumgartner, A., Cabrera-Perez, D., Frank, F., Gromov, S., Grooß, J.-U., Harder, H., Huijnen, V., Jöckel, P.,
755 Karydis, V. A., Niemeyer, K. E., Pozzer, A., Riede, H., Schultz, M. G., Taraborrelli, D., and Tauer, S.: The community atmospheric chemistry box model CAABA/MECCA-4.0, *Geosci. Model Dev.*, 12, 1365–1385, doi: 10.5194/gmd-12-1365-2019, 2019.

- Sobanski, N., Schuladen, J., Schuster, G., Lelieveld, J., and Crowley, J. N.: A five-channel cavity ring-down spectrometer for the detection of NO₂, NO₃, N₂O₅, total peroxy nitrates and total alkyl nitrates, *Atmos. Meas. Techn.*, 9, 5103–5118,
760 doi:10.5194/amt-9-5103-2016, 2016.

Sillman, S., Al-Wali, K., Marsik, F. J., Nowacki, P., Samson, P. J., Rodgers, M. O., Garland, L. J., Martinez, J. E., Stoneking, C., Imhoff, R., Lee, J. H., Newman, L., Weinstein-Lloyd, J., and Aneja, V.: Photochemistry of ozone formation in Atlanta, GA - models and measurements, *Atmos. Environ.*, 29, 21, 3055–3066., doi:10.1016/1352-2310(95)00217-M, 1995.

- 765 Thornton, J. A., Wooldridge, P. J., Cohen, R. C., Martinez, M., Harder, H., Brune, W. H., Williams, E. J., Roberts, J. M., Fehsenfeld, F. C., Hall, S. R., Shetter, R. E., Wert, B. P., and Fried, A.: Ozone production rates as a function of NO_x abundances and HO_x production rates in the Nashville urban plume, *J. Geophys. Res.*, 107, D12, doi:10.1029/2001JD000932, 2002.



770 Tuzson, B., Zeyer, K., Steinbacher, M., McManus, J. B., Nelson, D. D., Zahniser, M. S., and Emmenegger, L.: Selective measurements of NO, NO₂ and NO_y in the free troposphere using quantum cascade laser spectroscopy, *Atmos. Meas. Tech.*, 6, 927-936, doi:10.5194/amt-6-927-2013, 2013.

Viallon, J., Lee, S., Moussay, P., Tworek, K., Petersen, M., and Wielgosz, R. I.: Accurate measurements of ozone absorption cross-sections in the Hartley band, *Atmos. Meas. Tech.*, 8, 1245-1257, doi:10.5194/amt-8-1245-2015, 2015.

775 Velchev, K., Cavalli, F., Hjorth, J., Vignati, E., Dentener, F., and Raes, F.: Ozone over the Western Mediterranean Sea – results from two years of shipborne measurements, *Atmos. Chem. Phys.*, 11, 675-688, doi:10.5194/acp-11-675-2011, 2011.

Zhou, W., Cohan, D. S., and Henderson, B. H.: Slower ozone production in Houston, Texas following emission reductions: evidence from Texas Air Quality Studies in 2000 and 2006, *Atmos. Chem. Phys.*, 14, 2777-2788, doi:10.5194/acp-14-2777-2014, 2014.

780